Petrography of impactites from the Dellen impact structure, Sweden

Robert Mroczek

Dissertations in Geology at Lund University,
Master's thesis, no 648
(45 hp/ECTS credits)

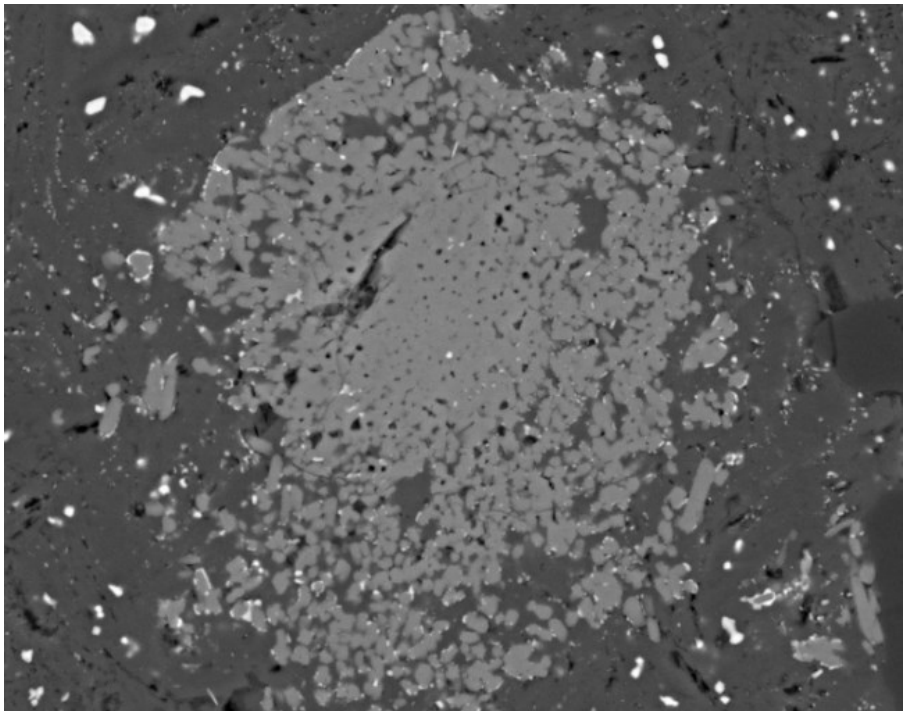

Department of Geology
Lund University
2022

Petrography of impactites from the Dellen impact structure, Sweden

Master's thesis

Robert Mroczek

Department of Geology
Lund University
2022

Contents

Cover Picture: Fractured, shock-recrystallized apatite grain in an impact melt rock from the Dellen impact structure, Sweden (thin section 3CH). Viewed in back-scattered electrons (BSE). Taken by Robert Mroczek.

Petrography of impactites from the Dellen impact structure, Sweden

Robert Mroczek

Mroczek, R., 2022: Petrography of impactites from the Dellen impact structure, Sweden. *Dissertations in Geology at Lund University*, No. 648, 46 pp. 45 hp (45 ECTS credits).

Abstract: Identification and characterization of shock-metamorphic features in hypervelocity impact craters is important for our understanding of how shock waves interact with geologic materials and how impact craters form, which in turn is essential to our understanding of what role impact cratering played in the development of our solar system. Of particular interest are accessory minerals like apatite, which contains various volatiles that can affect the atmosphere of a body, or magnetite whose magnetic properties constitute a remote sensing indicator which allows us to study and understand the internal structures of distant bodies. Understanding how these magnetic properties are affected by shock waves in impacts allows for better modelling and interpretation of data retrieved by remote sensing. This study reports on multiple examples of shock-metamorphic features from allochthonous samples retrieved from the Dellen impact structure, Sweden. Shock-metamorphic features chiefly in apatite and magnetite, but also zircon, titanite, biotite, quartz and feldspar are reported on. Apatite and magnetite grains were both found to show signs of dynamic recrystallization, and apatite also displays tentative micro-vesicles. Other shock-metamorphic features identified include 'ballen quartz' and baddeleyite formation in zircon. Some features were also found which may have been induced by the shock waves, but whose origins are unclear, such as exsolution textures in titanite.

Keywords: Dellen, Impact, structure, magnetite, apatite, shock waves, shock-metamorphic, features, Impactite, petrography, scanning electron microscope, SEM, geology.

Supervisor(s): Sanna Alwmark, Carl Alwmark.

Subject: Planetary geoscience, mineralogy

Robert Mroczek, Department of Geology, Lund University, Sölvegatan 12, SE-223 62 Lund, Sweden. E-mail: Robban.mroczek@gmail.com

Petrografi av impaktiter från impact strukturen i Dellen, Sverige

Robert Mroczek

Mroczek, R., 2022: Petrografi av impaktiter från impact strukturen i Dellen, Sverige.

Examensarbeten i geologi vid Lunds universitet, Nr. 648, 46 sid. 45 hp.

Sammanfattning: Identifiering och karaktärisering av chock-metamorfa strukturer i nedslagskratrar är viktigt för vår förståelse av hur chockvågor interagerar med geologiska material och hur nedslagskratrar bildas, vilket i sin tur är essentiellt för att förstå rollen meteoritnedslag har spelat under vårt solsystems utveckling. Accessoriska mineral är av speciellt intresse. Två av dessa är Apatit, vilket innehåller volatiler som kan påverka atmosfären på en kropp, och magnetit, vars magnetiska egenskaper är viktiga för fjärranalys. Att förstå hur dessa magnetiska egenskaper i magnetiska mineral förändras efter att ha utsatts för chockvågor tillåter bättre modellering och tolkning av fjärranalys-data. Denna studie rapporterar flera exempel på chock-metamorfa strukturer i alloktona prover insamlade från nedslagskratern Dellen i Sverige. Chock-metamorfa strukturer rapporteras framför allt i apatit och magnetit, men även zircon, titanit, biotit, kvarts och fältspat. Både apatit och magnetit har blivit granulära, medan apatit även innehåller mikro-vesikler och potentiella tecken på att avgasning har orsakat frakturering av apatitkorn. Andra chock-metamorfa strukturer som hittats inkluderar ’ballen kvarts’ och baddeleyit-formation i zircon. Andra strukturer som också kan ha orsakats av chock-vågorna men som är osäkra inkluderar utfällningstexturer i titanit.

Nyckelord: Dellen, Impakt, struktur, magnetit, apatit, chock, chockvåg, chock-metamorf, Impaktit, petrografi, SEM, geologi, krater, nedslagskrater.

Handledare: Sanna Alwmark, Carl Alwmark.

Ämne: Planetär geovetenskap, mineralogi

Robert Mroczek, Geologiska institutionen, Lunds Universitet, Sölvegatan 12, 223 62 Lund, Sverige. E-post: robban.mroczek@gmail.com

1. Introduction

Microscopic shock-metamorphic features are of great importance to our understanding of how hypervelocity impacts have affected the geology and atmosphere of bodies in our solar system. The impact structures themselves can measure hundreds of kilometres across, and the extreme pressures produced at the impact point can exceed 500 GPa. This pressure change travels outward from the impact point in the form of shockwaves. Such extreme pressure changes lead to heat release, near-instant vaporization and high pressure/temperature metamorphism of large volumes of rock. The shock waves leave irreversible effects in various minerals which are unique to rocks exposed to shock waves. Also produced in the impacts are new rock types and large morphological disturbances (French, 1998).

The most direct way to study the effects of these events on the target bedrock are polarizing microscopy and scanning electron microscopy (SEM). Historically, identification and analysis have been done using polarizing microscopes. These studies have allowed for diagnostic identification of meteorite impact craters by the finding of (among other features) shock-produced planar deformation features (PDFs) in quartz (SiO_4) grains which is one of the most commonly found shock-metamorphic features.

Using SEMs, we have the ability to look at a variety of features which polarizing microscopes cannot. Two mineral groups whose habits under shock exposure have previously been poorly studied are calcium phosphates and magnetic minerals.

Calcium phosphates such as apatite ($Ca_5(PO_4)_3$ (F,Cl,OH)) contain a number of volatiles including fluorine, chlorine and water. These volatiles have the potential to be mobilized during impact, but little research has been conducted on how apatite reacts to shock waves. The elemental abundance and isotopic ratios of the volatiles contained in calcium phosphates and how they are mobilized, is relevant to our understanding of the geology of other bodies such as Mars, where they can be used to uncover the magmatic history of the planet (Filiberto & Treiman, 2009; McCubbin *et al,* 2012; Shearer *et al*. 2015).

Magnetic minerals in general, but chiefly magnetite (Fe_3O_4) and pyrrhotite ($Fe_{(1-x)}S$)(Reznik *et al*, 2016) are of interest because their magnetic properties constitute a way for remote sensing the mineralogy of rocks in areas both on Earth and on extraterrestrial bodies such as Mars. Magnetic minerals' properties have been shown to be permanently altered following exposure to shock waves (Gattacceca *et a*l, 2006, 2010; Bezaeva *et al*, 2007). Multiple studies have shown that shock waves can diminish or erase remanent magnetism in magnetic minerals (Reznik *et al*, 2016; Kontny *et al*, 2018). Characterizing these magnetic minerals´ recrystallization habits when subjected to shock waves provides additional understanding of the magnetization patterns associated with impacts.

Nine thin sections from the Dellen impact structure, Sweden, have been examined using a polarizing microscope and a SEM equipped with a back-scattered electron (BSE) detector and an energy dispersive x-ray detector (EDS or EDX). This study focuses on the microscopic features which are left by the powerful shock waves generated during the brief moments of impact. The aim is to improve our knowledge of how various accessory phases react in response to shock waves, with a particular focus on apatite and magnetite.

2. Background

2.1. The origins of meteorites

Hypervelocity meteorite impacts are recognized today as an important process in the geological development of all solid bodies in our solar system. Not only do they change the morphology of bodies, but may also affect their bulk chemistry. Shock-metamorphism caused by meteorite impacts could also be an important factor in the formation of planetary atmospheres (French, 1998).

A meteorite is a body of silicate rock, metal or a mixture of the two, which has impacted Earth's surface from space. They originate from celestial bodies called asteroids, comets, planets or moons (Mcsween, 1999). Asteroids and comets both generally orbit the sun, but may also orbit planets. Asteroids are mainly made up of silicates and metals, while comets also contain ices of a variety of volatiles in addition to metals and silicates. These volatiles form a characteristic 'tail' of gas and dust as they warm up. The distinction between comets and asteroids can seem arbitrary since comets gradually lose their volatiles and as such transition into being asteroids if they lose all their volatiles. They are however generally thought to have different processes of formation. Asteroids generally represent fragments of larger bodies (called parent bodies or source bodies) which exist or have existed previously in the solar system (Weisberg *et al*, 2006), and are thought to form in the inner solar system at distances closer than that of Jupiter's orbit. Comets on the other hand are believed to have formed out of material which was thrown far out into the outer solar system in the very early history of the solar system 4-4,5 billion years ago (European Space Agency, 2021).

Most meteorites found on Earth come from the 'Main asteroid belt' located between Mars and Jupiter, but the solar system also includes many other asteroid and comet cluster structures. Common ones to be mentioned include the Kuiper belt (located roughly 20 AU from earth) and the Oort cloud (2000 AU), which both consist of comets and are situated beyond the most distant planets of our solar system.

2.2. Meteorites as proxies for the young solar system

Meteorites are useful as proxies for the history of our solar system's development (Boynton, 1984). To date there are an estimated number between 100 and 150 extraterrestrial bodies thought to be the possible parent bodies of all meteorites found on Earth, which is a notably large discrepancy (Weisberg *et al*. 2006). The discrepancy can be attributed to differences in opinions as to how certain characteristics should be interpreted. Classification schemes rely on petrographic characteristics, mineralogy as well as whole-rock chemistry for metrics. But while these metrics may be accurate, it is the interpretation of this data which is

critical to a classification that makes sense within the context of solar system dynamics. An example of this are the parent bodies which are, in many cases, theorized to have existed based on similar mineralogical, petrographic and chemical characteristics which makes the idea of one common parent body probable, but could still feasibly represent multiple bodies of similar compositions, and as such require a different explanation (fig. 1) (Burbine *et al*, 2002).

There are also questions regarding what biases may affect our meteorite record, such as dynamics within the Main asteroid belt (from which 99,8% of meteorites found on Earth are thought to originate (NASA, 2006)), and the destruction of particularly fragile types of carbonaceous chondrites during atmospheric entry (Burbine *et al*, 2002; Sears, 1998).

Chondrites (and carbonaceous chondrites in particular) are the oldest and most compositionally like our sun's atmosphere (usually referred to as a "primitive" composition) of all meteorites (Wood, 1988). Although there are many types of chondrites, they all share the internal texture which is their namesake. The texture consists of characteristic chondrules found inside undifferentiated meteorites. The chondrules in different bodies vary in characteristics, and the origins of the chondrule texture is debated. Chondrites are generally thought to originate from the time that the solar system was just coalescing and planets were not fully formed yet, about 4,53 billion years ago (Wood, 1988). About 85% of all meteorites found on earth are chondrites (Meteoritical Bulletin Database, 2018).

Primitive achondrites, iron and stony-iron bodies are examples of Achondrites (fig 1). Achondrites consist of differentiated material (Weisberg *et al*, 2006), which means that they at some point were subjected to magmatic/metamorphic processes following the coalescence of large enough bodies in the solar system.

Large bodies approaching dwarf planet status (in the order of hundreds of kilometres in diameter) can sustain metamorphic and magmatic processes inside of them, producing fractionation. This gives rise to these differentiated bodies. In the case of iron meteorites, they are the broken up pieces of such planetesimals' cores.

Most bodies are small and cold, however. Because of their low temperatures, the progression of chemical processes inside of them is also slow. Effectively, the bulk chemistries as well as textures found today, can be viewed as proxies for the conditions of our solar system in the past, since they will not have changed much following their formation.

Some of these bodies orbits' may already intercept our planet's, while in other cases disturbances such as collisions with other bodies may cause them to be flung into a new trajectory on a collision course with Earth. At relative velocities of up to 72 km/s, large meteorites can penetrate Earth's atmosphere without breaking or burning up, leading to surface impacts and the formation of impact craters (Bland & Artemieva, 2003).

2.3. Hypervelocity impacts

In order for a hypervelocity impact to occur, a projectile must have enough mass and speed to maintain its original cosmic speed until it reaches the surface. The main factor working on a body passing at high speed through the atmosphere is friction. As the amount of friction scales with surface area, this means that having a high mass relative to surface area increases the odds for a body to survive the journey through the atmosphere. If the impact velocity is subsonic relative to the target rocks, then no shock waves form and the crater will be no larger than a few meters. This means that the projectile needs to exceed a size of about 50m in diameter for a rocky body, or 20m for an iron meteorite (Bland & Artemieva, 2003) to impact Earth's surface at hypersonic velocity. This also means that unconsolidated bodies are at a disadvantage. Because when they break, their effective surface area is increased. The larger the surface area, the greater the slowing effect of the atmosphere. The relative speed at which they impact varies between 11 km/s and 72 km/s. The big difference in impact velocity is highly dependent on the directionality of movement and speed of Earth (roughly 30km/s around the sun).

Upon impacting the surface, the projectile pierces about 1-2 times its own diameter into the ground before its kinetic energy is fully converted into shock waves (French, 1998). The shock waves propagate both through the projectile itself and the surrounding bedrock in a concentric manner, causing the formation of a crater (more on crater formation further on). The first and immediate effect of an impact is a compres-

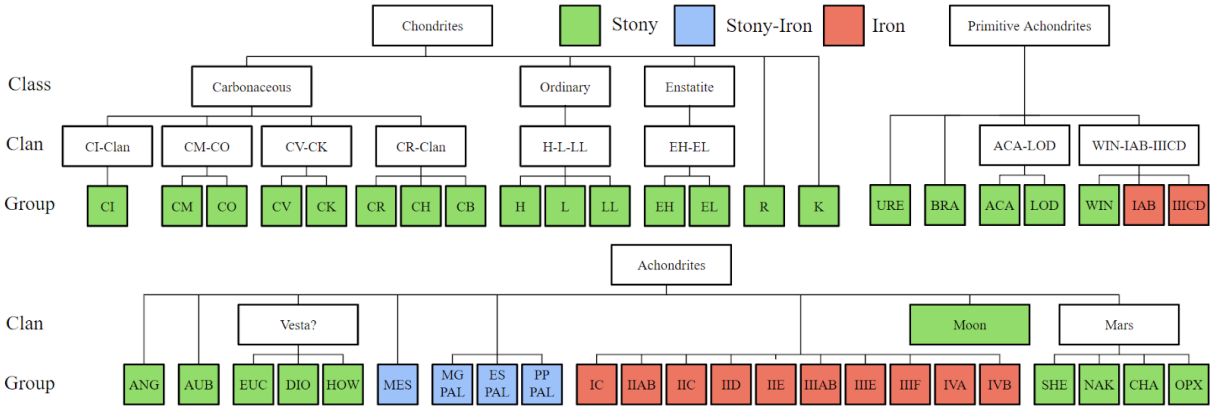

Figure 1. A scheme of meteorite classification showing tiers of divisions called classes, clans and groups. While there is often considerable overlap between classification schemes, from the clan-level and down, there is uncertainty as to the significance of their mineralogical, petrographic and chemical differences. Illustration from Weisberg *et al* (2006).

sion of volume in the nearby affected rocks.

The resultant increased pressure prevents the immediate melting of the pressurized material. It is under these extreme conditions and in this brief moment that minerals may quickly deform or transform into new high-pressure phases in response.

Following the compressive shock wave is the decompressive rarefaction wave. It is during decompression that most heat is generated and the depressurization to ambient pressure allows for temperature-controlled processes such as decomposition of volatile -bearing minerals, melting and vaporization/ sublimation to occur.

It is a commonly held belief that all meteorites are nearly completely vaporized during hypervelocity impacts. However, modelling has suggested that for impact angles <45° and velocities of 20 km/s, less than 50% of the impactor's mass is vaporized (Pierazzo and Melosh 2000). The remaining mass stays either solid or liquid, and is either incorporated into the resulting impact melt or thrown into the air and deposited on top and on the sides of the crater, creating a characteristic ejecta blanket.

2.4. Identifying hypervelocity impact sites

Craters are often recognized by the structure of the surrounding ejecta blanket, or by finds of meteoritic fragments. However, these features are not sufficient to conclusively identify an impact structure. While "fresh" hypervelocity impact craters' morphologies are recognizable by the naked eye, the older and the smaller the crater is, the more erosion and other processes affect any given surface structure. For highly eroded structures which may not have easily identifiable surface features, microscopy of the affected rocks is required. Finding microscopic shock-metamorphic features such as PDFs in quartz is considered unambiguous proof of extraterrestrial impact origin. Rocks containing such features are called impactites. There are many subtypes of impactite based on location, degree of melting, brecciation, etc (fig. 2).

Shock waves generated during the impact can permanently alter the crystal structures of many minerals in multiple ways which are diagnostic to meteorite impact sites (French & Short, 1968; French, 1968a, 1990b). Some of these features can be recognized in thin sections under a polarizing microscope, while others may only be seen by using electron microscopy.

Other than petrographic features, chemical analysis can also be used to identify impact sites. Hypervelocity impacts generally lead to the formation of an impact melt sheet. The amount of energy released into both the target rocks and the projectile itself during a hypervelocity impact inevitably leads to the partial mixing of the projectile into the resulting impact melt sheet, contaminating the original elemental bulk composition.

The impact melt sheet is where the highest ratio of meteorite contamination is found, and generally in close proximity to the point of impact. But examples of highly contaminated ejected melt also exist (Alvarez *et al*, 1980; Smit and Hertogen, 1980). This extraterrestrial material contamination can be identified by their contents of siderophile elements

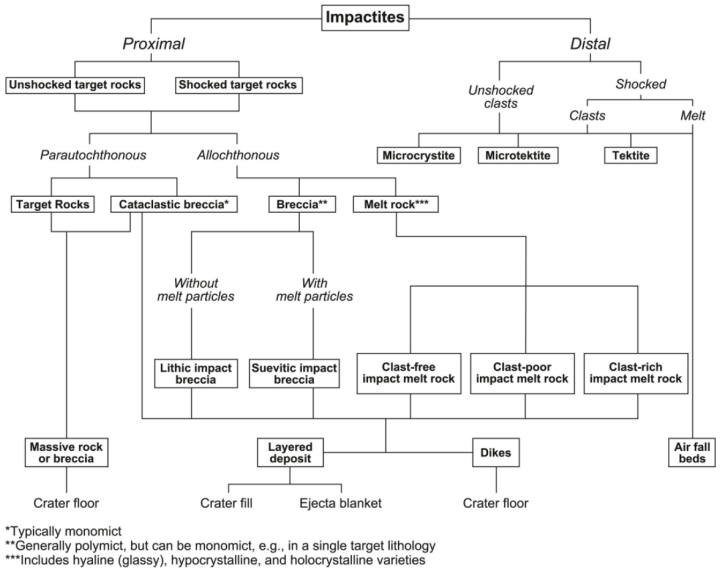

Figure 2. Scheme of the latest impactite nomenclature. From Stöffler *et al* (2018).

(Sometimes also called impact related elements (IRE's)), which are very uncommon in the Earth's crust, and/or isotopic composition. IRE elements include iridium (Ir), osmium (Os), ruthenium (Ru), rhodium (Rh), platinum (Pt) and palladium (Pd)) as well as nickel (Ni) and chromium (Cr).

By comparing the chemistries and isotopic data of the unaffected surrounding bedrock and the impactites, the fraction of meteorite material can be calculated (also depending on the type of impactor).

2.5. The cratering process

The process of crater formation is generally considered to consist of three distinct stages. The contact and compression stage, the excavation stage and finally the modification stage (Gault *et al,* 1968).

In literature, the terms "transient crater" or "transient cavity" are used. They are used to denote two different points in time but are used interchangeably which can cause confusion. The first usage refers to the moment right after the crater is fully formed and before any settling or erosion had time to occur (Turtle *et al*, 2005). The second usage refers to a moment in time in which the crater has its largest spatial extent. After which gravity takes over and mass movement momentum reverses to settling, rather than flying away.

Because of this ambiguity in word usage, it is worth pointing out that it is the latter which is used in this work. The transient crater size is calculated using what we know about the evolution of craters over time, in order to determine how energetic the impact was.

Real world scenarios differ from this idealized scenario depending on local conditions where the impactor hits. For example, the projectile in the following figures impacts the surface at a perfectly perpendicular angle (fig. 3 and 4). If the impact occurs at an angle, which will be the case in the vast majority of real-world scenarios, the net mass movement can be heavily skewed in the direction that the projectile was traveling relative to the surface (Pierazzo & Melosh, 2000).

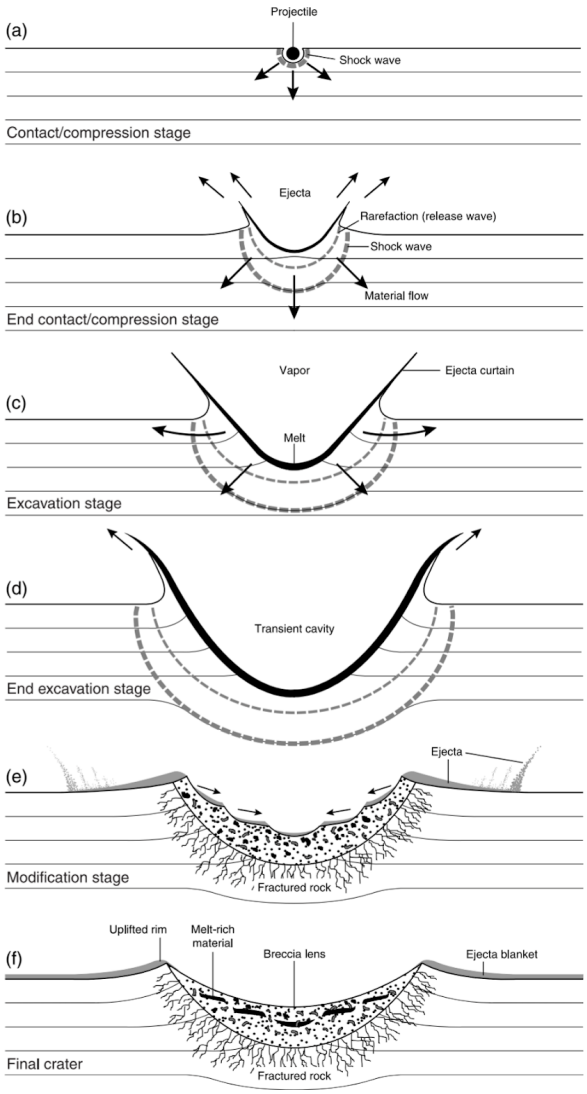

Figure 3: Illustration of the structure of a crater during its formation, marking the transitions between stages in chronological order from drawing 'a' to 'f'. (a) The impact and compression stage. The projectile pierces 1-2 times its diameter into the bedrock, forming a shock wave traveling outward. (b) The excavation stage. The rarefaction wave follows the shock wave and causes the vaporization of the projectile along with mass movements (see fig 3 for more). The initial shockwave also reaches the ground surface, being partially reflected and launching near-surface ejecta into the air. (c) the combined mass movements of both ejecta and subsurface rocks within the crater both combine to expand outward and upward. (d) the transient crater is formed, marking the moment after which the structure starts to settle and ejecta falls to the ground. The shock waves subside. (e) The modification stage begins. Ejecta is settling on the sides of the crater and the steep sides of the crater slump into the crater centre at the same time. The mixing of the two forms breccia lenses (mixed breccias) within the crater. steps 'a' to 'e' all occur within seconds. (f) Within minutes to hours, the crater structure is complete. Slumping will continue to occur at lower rates, but from here on out, erosional processes take over the development of the structure. Illustration from French (1998).

2.5.1. The contact and compression stage

In the contact and compression stage, the projectile first makes contact with the surface. The projectile itself pierces into the surface (see fig. 3). The kinetic energy of the projectile is converted into a shock wave which travels outward concentrically. By the time it pierces about 1-2 times the diameter of the projectile into the ground, the kinetic energy is completely converted into a shock wave (French, 1998). The shock wave propagates through both the projectile and the target rock originating from the contact surface of both units. Upon the shock wave reaching the upper surface of the projectile, a rarefaction wave travels in the opposite direction of the shock wave, relieving the pressure and causing the conversion of the released energy into heat and other forms of energy.

The pressure release and subsequent conversion into heat will vaporize and/or melt the impactor along with bedrock in close proximity. The grade of melting in the bedrock decreases with distance from the impact, as the shock wave spreads its energy over a greater area (French, 1998).

2.5.2. The excavation stage

The shock waves generated by the projectile as it pierces into the ground carry the immense energy of the projectile into the surrounding rocks, resulting in complex interactions which breaks and pushes away the surrounding rocks in a roughly hemispherical area around the impact spot (see fig. 4). The base of this upside down dome-shape of shock expansion is at the maximum depth of penetration for the projectile. The physical projectile itself does not play a role in the actual crater formation (French, 1998).

Shock waves which originate from below the original ground level travel toward the ground surface. Upon reaching the free surface, the shock wave is reflected back as a pressure release wave into the surrounding bedrock again, resulting in tensile stresses in addition to the compressive stress from the shock wave.
Complex wave interactions of shock waves and pressure release waves ultimately result in a net mass movement upward and outward radially from the impact site, varying with the initial position inside the crater area.

The energy carried by the shock waves is enough to accelerate a large area around the projectile, meaning that the crater size will be much larger than the projec-

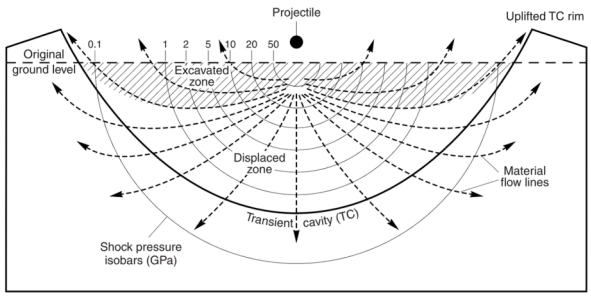

Figure 4. drawing illustrating mass movement and the pressure zones (GPa) of the shock wave as it travels outward. The bedrock is pushed down in the centre and progressively more outward and upward the further from the impact site. Excavated material is marked by grey lines. The movements cause the excavation of the impact site and creation of a crater rim which is topographically higher than the original ground level (From French, 1998).

tile itself. The determining factors for crater size is the target material characteristics and kinetic energy released upon impact, which is dependent on the mass of the impactor as well as the relative velocities of earth and the impactor. Generally, a hypervelocity impact crater size is about 20x the size of the impactor on Earth. But crater sizes can be up to about 30x the size of the impactor in the case of the most dense impactors which are iron meteorites (French, 1998).

Shock waves deposit their energy quickly into the medium through which they are propagating. This quick conversion of shock waves into soundwaves, kinetic energy and heat energy simultaneously make the impact extremely violent and short-lived.

The excavation stage only lasts for up to a couple of minutes, even for the largest of craters. At the instant that the shock waves lose enough energy that they can't break or displace any more rock, the excavation stage is over and the modification stage begins.

2.5.3. The modification stage

The modification stage is defined by gravitationally controlled processes and erosion. The completed form of the crater is gradually broken down during this stage. It also lasts much longer than the other stages of crater formation. The duration can be considered ambiguous as it would depend upon where you draw the line between ordinary geological processes and impact-related ones (French, 1998). During this stage, the crater is compactified by gravitational settling of fragments and infilling of cavities. Weather erodes any topological features and the crater walls quickly slump into the crater. The impactites also cool and crystallize.

2.6. Craters

2.6.1. Simple craters

The smallest hypervelocity impact craters are the simple craters. Their structures are essentially the same as the shape of the transient crater. The defining features include a steep inner wall, a nearly half-spherical inner bowl shape and a filling of interchanging layers of both shocked, unshocked and brecciated material along with lenses of impactite of varying degrees of melting. The only main modification that occurs to a simple crater's structure, is a high degree of sidewall collapse. The slumping of this material into the crater effectively increases the diameter of the bowl over time. As such, old simple craters' diameters can appear up to about 20% larger than their original size on the surface level (French, 1998).

2.6.2. Complex craters

More energetic impacts create inward and upward mass movements in the centre of the structure, quickly leading to the uplift of the subcrater rocks and emergence of a central uplift in the structural middle. Within minutes of impact, the central uplift is fully formed (French, 1998).

The height of this uplift above the crater floor is roughly equal to 10% of the excavation depth on Earth (Grieve & Pilkington, 1996). Crater size and central uplift formation are however inversely correlated with gravity. On Earth, central uplift structures start to form in craters sized 2-4 kilometres in diameter depending on the type of target rock (uplift structures form more readily in sediments than in solid crystalline material, for example). On bodies with lower gravity these structures require larger craters than they do on Earth, to produce the same uplift height. On the moon, which has approximately 16,6% of earth's gravity, such central uplifts start to form in craters of about 15-20 km in diameter (French, 1998).

Large complex craters may also be called 'peak ring craters', as the structure may instead develop a circle-shaped structure surrounding the centre (Pike, 1988). The formation of this circular structure gradually replaces the central peak.

Particularly large craters (hundreds of kilometres in diameter) may contain multiple ring-structures and are sometimes also devoid of central peaks. In such cases, they are called 'multi-ring basins'. How the impactor and the target's compositions along with the target's internal structure affect the transition to a multi-ring basin cannot be fully explained by current models (Potter, 2015).

2.7. Shock-metamorphic effects

Other than melted material and fracturing, a hypervelocity impact also leaves other effects in parts of target rocks which did not fully melt or vaporize. These are the results of the powerful shock waves. On the largest scales, of hundreds of meters there are cracks. Then there are shatter cones on the scales of metres. Shatter cones (formed between 2-6 GPa) are the only shock-metamorphic feature visible to the naked eye, and are also considered diagnostic of hypervelocity impacts.

On microscopic scales there are small but pervasive perturbations in the crystal lattices of quartz, mica and other minerals, which are visible in a polarizing microscope, called planar deformation features (PDFs). PDFs start appearing above pressures of about 10 GPa in nature. High-pressure polymorphs form over a wide range of pressures depending on the mineral, and at pressures between 22-80 GPa, diaplectic glasses are arguably the final known feature to appear before the complete melting of a rock. Impact pressures and temperatures associated with extraterrestrial

Characteristic	Regional and Contact Metamorphism; Igneous Petrogenesis	Shock Metamorphism
Geological setting	Widespread horizontal and vertical regions of Earth's crust, typically to depths of 10–50 km	Surface or near-surface regions of Earth's crust
Pressures	Typically <1–3 GPa	100–400 GPa near impact point; 10–60 GPa in large volumes of surrounding rock
Temperatures	Generally ≤1000°C	Up to 10,000°C near impact point (vaporization); typically from 500° to 3000°C in much of surrounding rock
Strain rates	10^{-3}/s to 10^{-6}/s	10^{4}/s to 10^{6}/s
Time for completion of process	From 10^{5}–10^{7} yr	"Instantaneous": Shock-wave passage through 10-cm distance, $<10^{-5}$ s; formation of large (100-km-diameter) structure <1 hr
Reaction times	Slow; minerals closely approach equilibrium	Rapid; abundant quenching and preservation of metastable minerals and glasses

Table 1. Comparing "normal" geological processes to those in impact events. "normal" geological metamorphic conditions and timescales on the left, and those seen in hypervelocity impact events on the right. From French, 1998.

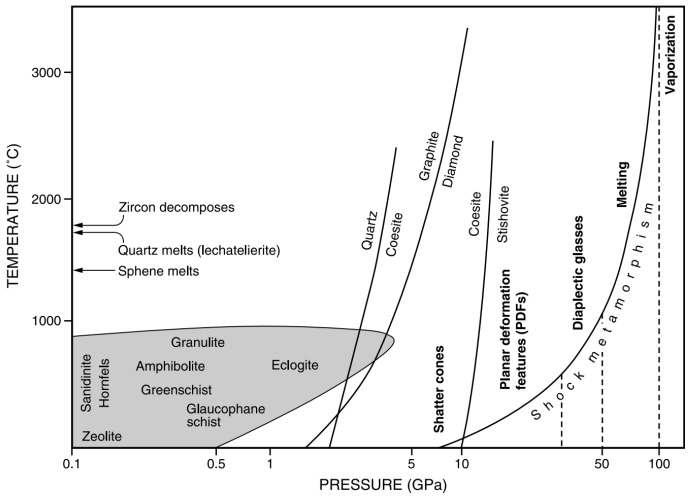

Figure 5. A plot showing the pressures (on a logarithmic scale) and temperatures associated with rock-forming minerals, along with shock-metamorphic features. The grey infilled area contains the metamorphic facies which roughly represent the range of P-T that rocks and minerals formed by "ordinary" terrestrial processes experience. Approximate stability lines of notable reactions such as the formation of diamond, the transitions of quartz polymorphs coesite and stishovite as well as diagnostic shock-effects like PDFs in quartz are also marked. From French (1998).

hypervelocity impacts far exceed typical conditions associated with rocks or minerals found in other contexts on the Earth's surface (Table 1), as shown in figure 5. Below are explanations of the common shock-metamorphic features.

2.7.1. Dynamic recrystallization

Dynamic recrystallization is a general process which occurs in shocked materials. Dynamic recrystallization of a solid material occurs due to high strain. The process allows for immediate recrystallization, and does not require heat from the surroundings during deformation as opposed to static recrystallization (McQueen, 2003). The process results in the creation of multiple sub-grains which can have other orientations and sizes than the original grain. The resultant appearance is why it's often referred to as 'turning granular'.

2.7.2. Kinkbanding

Kinkbands are a low-grade shock-metamorphic feature found in most craters containing mica. Formed in tabular minerals, kinkbands are the product of high strain. Because of mica's tabular crystal shape, this strain results in a very localized and regularly spaced deformation resulting in the folding of the originally straight "sheet" shape into an "S"-shaped kink inside of which the crystal can be heavily cracked, while the rest of the crystal can look unaffected (fig. 6). Kinkbands are not considered diagnostic for impact environments, although they are unusual in other contexts (French, 1998).

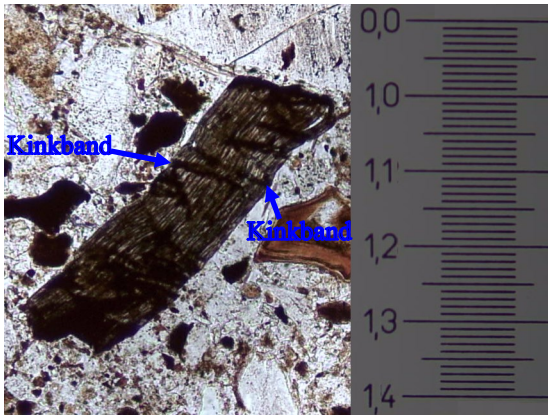

Figure 6. A biotite grain from thin section 3SC which displays kinkbands (multiple dark bands throughout the grain). Scale measured in millimetres.

2.7.3. Planar fractures (PF's)

Although they can visually look similar to PDFs, planar fractures have little else in common with PDFs. PFs are fractures, and are formed as a result of high shear stress. Because of this, they are most likely to be formed at a 45 degree angle to the crystallographic planes where shear stresses are highest, contrasting PDFs which form parallel to the crystallographic planes. PFs are also not continuous, meaning that they can span only a fraction of the subject grain's length, and are also not necessarily straight in nature since they follow zones of physical weakness.

2.7.4. Planar deformation features (PDFs)

PDFs are thin zones of diaplectic glass (see below) in the crystal lattice of individual grains. They have been most studied in quartz, but can form in many minerals. They cannot be seen with the naked eye, but are easily noticed in a polarizing microscope due to them changing the way light can pass through them.

They appear as straight, regularly spaced (2-10 μm), thin and black lines which run through the entire length of the grain (fig. 7). They start forming at dynamic pressures of about 10 GPa. PDFs are exclusively a product of shock wave deformation and are considered diagnostic of a meteorite impact when found in nature. The perturbations within each individual crystal are parallel to certain crystallographic planes. The specific planes vary between minerals. Multiple sets of PDFs can appear within a single crystal in different crystal planes. Multiple sets of PDFs are generally associated with higher magnitudes of shock absorption (Stöffler, 2018).

PDFs do not form in all minerals. Some minerals can transition into a new phase and others cannot, given a certain pressure, temperature and composition. This is largely determined by a combination of the kinetics of the transition from one crystal structure to another, and the pressure/temperature stability fields of any potentially new crystal structures/phases.

Figure 7. Example of A highly shocked quartz grain displaying numerous PDFs. Each black line represents a glassy zone within the crystal lattice and can be tracked through the entire length of the grain along a single crystallographic axis. Many PDFs are also 'decorated' (French 1969; Fig. 7a), which appears as tiny black sub-grains concentrated along the PDFs. The particular grain is not from Dellen. The image is modified from Mroczek (2014).

A transition must be able to occur quickly, due to the near-instantaneous pressure-changes associated with shock waves. In some minerals, transitioning to an alternate crystal structure can occur smoothly and quickly, which simply results in a new high-pressure crystalline phase being formed. However, in the cases of PDF-forming minerals, such a transition cannot occur efficiently under the given conditions and instead results in localized deformation within the grain, forming thin bands of diaplectic glass within the already present crystal lattice (Goltrant, 1992).

2.7.5. Diaplectic glass

The formation mechanism and conditions needed for grain-wide formation of diaplectic glasses in natural rocks is not well agreed upon. Suggested conditions for its formation vary between 22-80 GPa and differ by roughly 1000°C in temperature (Stöffler *et al*, 1986; Sharp *et al*, 1999; Chen & El Goresy, 2000; Kubo *et al*, 2010; El Goresy *et al*, 2013). In lab conditions, it has been shown to form at as low as 24 GPa in room temperature (Fritz *et al*, 2019). Diaplectic glass is similar to normal glass in that it is an amorphous phase, but different in that grain boundaries, zonations and bulk composition of the original mineral is retained. The density and refractive index of a diaplectic grain are also lower than the original mineral but higher than glass (Bunch *et al*, 1967; Engelhardt *et al*, 1967; Osinski *et al*, 2018). Diaplectic grains also display annealing behaviour (Stöffler, 1984).

The precise mechanisms resulting in diaplectism outside of laboratory conditions are still under debate. However, it is clear that it forms as a response due to the atomic structure of certain minerals not being able to neither maintain its current structure, nor rearrange into an alternative stable structure quickly enough, leaving a glassy state as the only option (Goltrant, 1992).

Diaplectism has been experimentally induced in quartz at pressures as low as 5 GPa in porous sandstone, and fully isotropic plagioclase feldspars (also called maskelynite) at above 24 GPa (Kowitz *et al*, 2013; Fritz *et al,* 2019). Grains are commonly only partially diaplectic, and appear as isotropic zones in an affected grain.

2.7.6. High-pressure mineral polymorphs

Polymorphs are minerals which share a chemical composition, but differ in their crystal structure. The crystal structure in turn is controlled by pressure and temperature conditions. Under any given such conditions, a certain few minerals are stable at any one time. This means that certain

minerals which require extreme pressures, temperatures or both to be stable and crystallize, are virtually never found on Earth's surface as terrestrial geological processes cannot provide the necessary conditions for them to form or be transported intact to the surface.

Hypervelocity impacts can however produce the necessary conditions. High pressures and temperatures generated during and after an impact give rise to the formation of high-pressure polymorphs in the near proximity of the impact. Such polymorphs commonly include coesite and stishovite (which are both polymorphs of quartz), jadeite (polymorph of albite), ringwoodite (olivine), diamond (graphite) and reidite (zircon).

The specific transformation mechanisms differ between minerals. Reidite has been shown to form at shock-pressures of 17,5-25 GPa in granitic rocks from the Chicxulub impact crater (Wittman *et al, 2021).*

Coesite, stishovite, jadeite and ringwoodite are examples of minerals which crystallize out of a liquid phase during decompression. Diamond formation on the other hand, is a solid state transformation by mechanism of martensitic shear (specifically during shock formation).

2.7.7. Ballen quartz

Ballen quartz is considered diagnostic of impact craters. Unlike most other known shock-metamorphic features, it is not directly produced by shock waves. Rather than being a unique mineral, "ballen quartz" is a texture (fig. 8) which specifically emerges post retrogression of high-pressure polymorphs of quartz such as lechatelierite, cristobalite (SiO_2), coesite and others, back into quartz (α-quartz).

Two formation "pathways" have been proposed (Ferrière *et al*, 2010). First, a solid-solid transformation from α-quartz to diaplectic quartz glass which then transforms into ballen of β-cristobalite and/or β-quartz at high temperatures, and finally retrogression into α-cristobalite and/or α-quartz. The second pathway involves the melting of the initial quartz phase in a solid-liquid transition from quartz to lechatelierite followed by nucleation and growth under high temperature, and later the regression back to α-quartz.

Because of the multiple precursor-phases, the incidence of ballen textures can represent a wide range of impact pressure and temperature (P-T) conditions. Ferriere *et al* (2008, 2009, 2010) proposed five categories of ballen quartz texture variations, of which they reported on types 1-4 were found in rocks from Dellen. Because the different precursor-phases represent such a wide range of conditions, ballen quartz is not a precise indicator of specific conditions beyond the minimum shock pressures required to form in crystalline rocks, which is ca 35 GPa, while it has been shown in experiments that ballen quartz can form at pressures as low as 5-12.5 GPa in porous, dry sandstone. (Ferriere *et al*, 2009).

2.7.8. Lechatelierite

Lechatelierite is a shock-produced vesicular pure silica glass which is normally found in sandstones (where it is formed by lightning strikes giving rise to extreme temperatures) or tektites, but are also found in impact melts where they instead form due to extreme pressures. In non-porous rocks, lechatelierite is found as schlieren and inclusions with flow textures.

Experimental studies on granitic rocks have indicated that impact pressures in non-porous rocks require shock magnitudes of 72,5-85 GPa to form lechatelierite, approaching the point of whole-rock melting (Schrand & Deutsch, 1998).

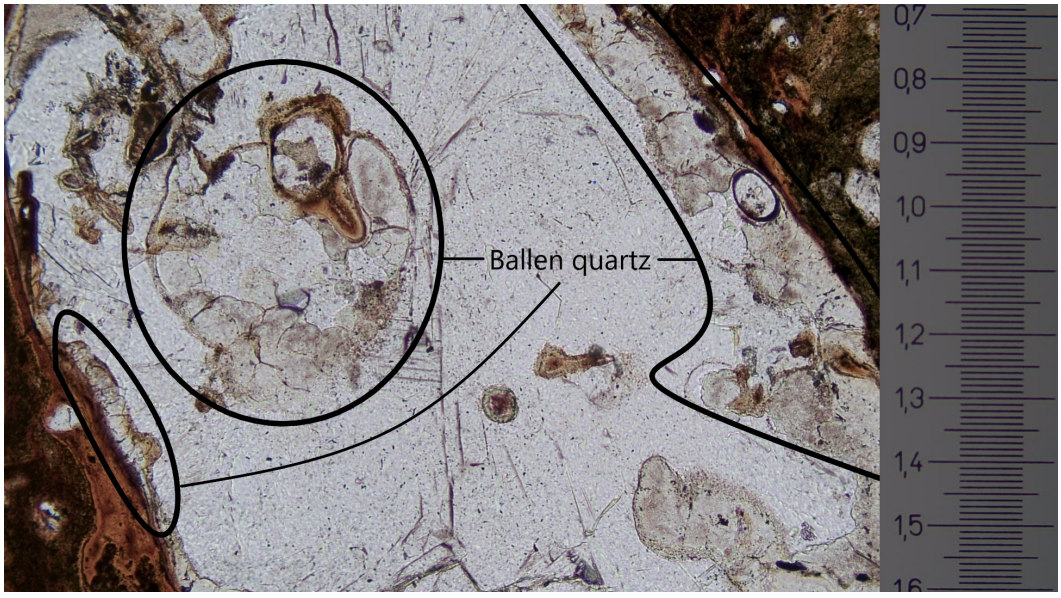

Figure 8. Example of the ballen quartz texture, circled in black. The texture consists of semi-circular, overlapping zones. Scale-bar in micrometres. In this case, the ballen are mostly a light brown colour and have a "dusty" appearance. The picture was taken in this study, in sample 3YB.

3. Geological setting and the Dellen impact structure

Located in central Sweden, the Dellen impact structure is a 20 km in diameter, 350 meter deep, circular structure which is largely filled with water (fig. 9). Due to the lake and flora covering most of the structure, few localities of exposed bedrock/ejecta blanket are available.

There is some disagreement on the degree of erosion that has affected the structure. Henkel (2010) described its state as well preserved, only marginally eroded, based on the extensive occurrences of impact melt in the structure. On the other hand, Deutsch *et al* (1992) and Lindström & Dalwigk (2002), describe the state of the structure as "highly eroded". Either way there are only a few localities where the structure can be studied on the surface.

Aeromagnetic measurements have indicated that there is a 9 km in diameter melt-bearing impactite sheet with a thickness of 200-500m (Delin, 1990; Henkel 1992) still left under the surface. Additionally, there is a superimposed grading -7 mGal anomaly across a large area coinciding with the structure, and a strong remanent magnetization present in the central parts of the structure (Henkel, 1992).

The structure has been dated using the Ar-Ar method to 140,82 ± 0,51 Ma (Mark *et al*, 2013).

It is defined as a complex impact structure due to the fact that it features a central uplift structure (more on central uplift structures below). A peninsula separates the water into two lakes. Sördellen to the south, and Norrdellen to the north (fig. 9; 10). The peninsula is called Norrbonäset, and is a part of the central uplift which has not been submerged.

The impactites in the area were considered peculiar for a long time before it was realized how they formed. In 1888, Svenonius described the rocks as 'volcanic' in nature, and later works labelled them as andesites which resembled those found in Lake Mien (Svenonius, 1895), another impact structure. The rocks were first suggested to be of an impact origin by Högbom in 1910. At the time, extraterrestrial impacts were generally not considered as a process which could cause significant geological structures (French 1998). Meteorites were known as curiosities which were found in museums. Naturally, the meteorites that people knew of at the time were the small ones. At the time, it was not realized that large meteorites are generally vaporized on impact. These small meteorites would form meter-sized pits, and not cause large-scale metamorphism. After 58 years, the findings of PDF's in quartz would prove that the rocks in Dellen had indeed been formed by a meteorite impact (Svensson, 1968).

Analysis of the meteorite contamination in Dellen has shown that the target rocks' chemical composition is virtually uncontaminated. Notable anomalies which have been identified include an excess of Ir (0.48 ± 0.23 ng/g, as to be compared to the average of 0,03 ± 0,02 ng/g in crustal rocks), as well as a low Os/Ir ratio for an impact structure. The levels of measured contamination indicated a nominal CI component under 0,1% (Schmidt, 1997). Because the contamination level is so low, no projectile classification for the meteorite that formed the Dellen impact structure exists to date. It is not even clear if it was an iron or stony-iron projectile which struck the area. It also means that all rocks within the impact structure can be considered nearly chemically equivalent to the surrounding Ljusdal granite.

The indigenous granitic rocks in which the crater is located are part of the Ljusdal batholith (which is part of the Sweco-karelian province), originally formed 1,84-1,86 Ga (Högdahl *et al*, 2008 and references therein) ago during the Sweco-karelian orogeny. Chemically, they are almost exclusively defined as granodiorite (fig.

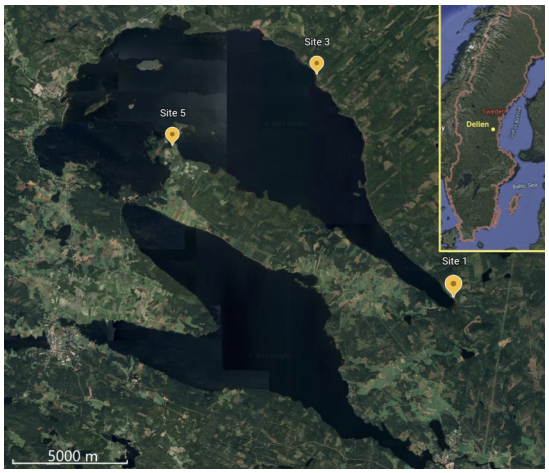

Figure 9. Composite image from Google Earth of the Dellen lakes. Their location within Sweden shown in the upper right corner, and with the sites where the samples used in the study were found marked.(Site 1, coordinates 61.817949, 16.875515, Site 3, 61.87574847434893, 16.648329412531456 and site 5, 61.90270726406089, 16.764641643038193)

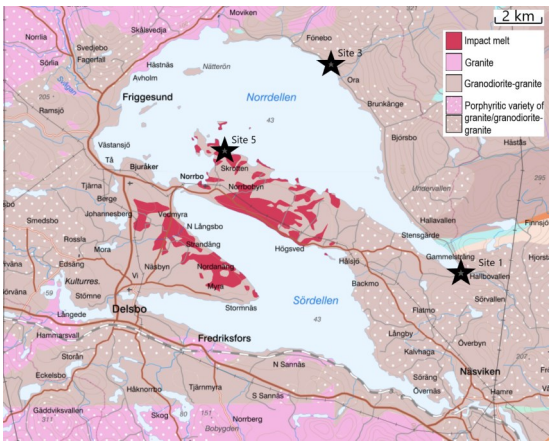

Figure 10. A colour-coded bedrock map displaying the types of rocks in the Dellen lakes area. Modified from bedrock maps retrieved from SGU (Swedish geological survey, 2021)

10). The rocks are mainly composed of quartz, feldspar, mica and magnetite. They also contain other minor phases such as titanite, zircon and apatite. Texturally, the rocks are porphyritic, and often schistose.

Looking at the impact structure on maps, the lakes are the defining feature. The lakes are however only the deepest part of the structure. While the bedrock peneplain surrounding the structure is located 200-300 meters above sea level, the bottom of the lakes is situated about 25 meters below sea level (Svensson, 1968). The diameter of the lakes is about 15 kilometres, and the actual topographic size of the structure in large is usually quoted as 20 km. The effects of the impact stretch further out than that, however. Henkel (1992) identifies features stretching out in a roughly 13 km radius around the structural centre. The bedrock textures within that purview can be divided into "rings" which are zones of modifications to the target rocks as measured by in situ resistivity measurements.

The outermost ring stretches from 13 - 8 km. At this distance, the rocks have mostly retained their texture and were classified as granitic breccias. An anastomosing network of thin (less than 1 cm thick) pseudotachylitic breccia veins can be found in the northeastern parts of the structure (Lindström & von Dalwigk, 2002). At 8 - 4,5 km from the centre, the bedrock is heavily brecciated, and classified as breccia. within 4,5 km of the centre, the bedrock is classified as an impact melt or impact melt breccia (sometimes also called Suevite) depending on the degree of melt (Henkel, 1992).

4. Methodology

4.1. Sample collection & naming

All of the samples used for this study are loose, allochthonous samples found on beaches close to the centre of the structure (Sites 1, 3 and 5 (fig. 9, 10)). The naming/labelling of the samples starts with a number corresponding to the order in which the locality was visited during sample collection. The following letters correspond to the order in which the sample was found. The final letter denotes each slice of the sample after sawing (meaning that sample 3CA was found in site 3, was the third sample found in that locality, and is the first slice of that sample). The slices were done in sequence. For example, slice 'A' always has a contact surface to Slice 'B' and 'B' has contact surfaces to slices A and C, et cetera.

After slicing the samples, they were examined by eye and prioritized. The amount of nine thin sections was chosen for reasons related to the cost of making them. Each chosen sample was then sent by package to an external lab in Poland, where the thin sections were made.

Once retrieved, each thin section was first examined using a polarization microscope and photographed, after which priorities were assigned to the samples for SEM analysis.

4.2. Thin section selection for SEM analysis

Four thin sections were examined for accessory phases. The specific thin sections in question (1AA, 3TA, 3CH and 3SC) were picked post lithographic studies to achieve a variety in mineral content and high degree of melting as well as comparing the differently coloured glasses. Thin sections containing highly shocked grains were preferred to maximize the chances of finding high-pressure polymorphs as well as other shock-metamorphic features.

Each thin section was first examined using BSE to find the specific phases of interest. After the BSE analysis, a small number of grains were picked for EDS analysis.

4.3. Scanning electron microscopy

The SEM analysis was performed on a variable pressure Tescan Mira3 High Resolution Schottky FE-SEM equipped with Oxford EDS and EBSD system and a CL system in the Geological institution of Lund University, Sweden.

Scanning electron microscopes emit a beam of electrons upon the target sample, which in turn interact with the sample in a multitude of ways. The interactions cause particle emissions which can then be measured by detectors inside the microscopy machine (Goldstein, 2003; McMullan, 2006). The techniques used for this study are Energy-dispersive X-ray Spectroscopy (EDS) and Back-scattered Electrons.

In using BSE, you measure the amount of primary electrons (sent out by the detector) which are either reflected or back-scattered (Goldstein, 2003; McMullan, 2006) when the beam hits the surface of the subject sample. Because of the binary nature of the measurement, the image will be black and white. The higher the amount of reflected/refracted electrons in a particular spot, the whiter the spot appears in the image. High-mass atoms refract more electrons than low-mass atoms, meaning that high-mass regions appear brighter in the final image. The resolution is determined by the wavelengths of the electrons which are sent out in the beam by the detector. Higher energies lead to shorter wavelengths and a higher resolution. The resolution using BSE is thus in practice limited, and cannot image single atoms. Because of this, the resultant shade of white reflects the average number of refracted/ reflected electrons in a small region.

EDS relies on the principle that each individual element has a unique electromagnetic emission spectrum (Goldstein, 2003). Upon excitation of the sample material caused by the electron beam, each element radiates a unique set of wavelengths of light (wavelengths typically associated with X-ray part of the spectrum, which is the method's namesake). They can then be detected and used to identify which elements are present in the sample and their relative abundances.

4.4. Impact nomenclature

The nomenclature of impact rocks has not historically been unified. Words such as suevite have not always been strictly defined, which means that the vocabulary usage in this work may differ from older works. The nomenclature used for this study is based on Stöffler *et al* (2018)(fig. 2).

5. Results

5.1. Sample 1A

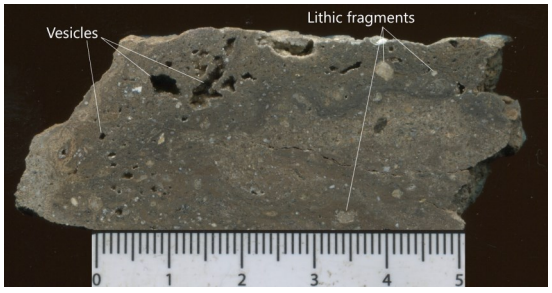

Figure 11. Sample 1A photographed in hand sample. Large vesicles can be seen (marked in white) surrounded by the glassy matrix. The matrix also contains a high fraction of lithic fragments which has not melted (also marked). The outermost layer of the sample has been exposed to the elements, and is markedly lighter (similar to a white eggshell in colour) than the inside of the sample. The scale bar is marked in centimetres.

Sample 1A (fig. 11) is nearly eggshell-white in colour on the surface which has been exposed to the atmosphere, and a significantly darker grey or brown on the inside. Among the studied samples, it is by far the lightest in colour in hand sample. It also contains vesicles 1-5 mm in diameter which are easily seen by the naked eye.

In thin section (1AA), the sample can be seen to have an intersertal texture (the angular spaces between individual crystals is occupied by glass) and consists of around 20-30% devitrified glass. Of the glass, an estimated 20% is orange to dark brown. The rest of the glass is light grey (fig. 12).

Mineralogically, the sample consists of major quartz, k-feldspar and plagioclase with minor biotite. Quartz grains are found with PDFs and in many cases toasted (giving them a dusty brown appearance, and as recrystallized quartz aggregates. Some of the brown glass has altered into spherulite and axiolite nucleating around mineral grain boundaries and there are also exsolution textures in some feldspar grains.

The SEM studies of thin section 1AA yielded no signs of shock-metamorphic features in any mineral other than quartz.

5.2. Sample 3A

The sample features vesicles up to 6 mm across,

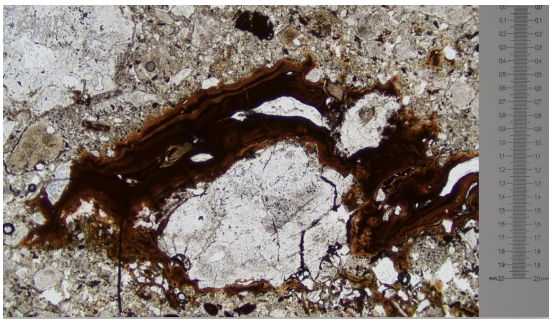

Figure 12. Photo of thin section 1AA in plane-polarized light (PPL) and 4x magnification. It shows the brown glass which occupies some 10% of the sample, surrounding a feldspar crystal. Flow textures are visible in the glass. Surrounding the glassy region are altered feldspar and quartz crystals with PDFs.

Figure 13. Sample 3A in hand sample after being cut. the sample contains vesicles up to about 6 mm across, and small lithic fragments up to about 2 mm across in a glassy matrix.

and lithic fragments up to about 2 mm across (fig. 13). The sample also has a millimetre-thick, light grey, weathered surface which was exposed to water and wind. This surface is much lighter in colour and more fragile than the inner parts of the sample which remain seemingly unaffected. The sample also has a lot of clearly visible vesicles which measure up to 6 mm across.

Thin section 3AG

Thin section 3AG features roughly 50% glass, of which all is light brown in colour. It also has strikingly regular spacing between melted clasts (fig 14). No shock-metamorphic features other than PDFs were observed in this thin section.

No SEM analysis was done on thin section 3AG.

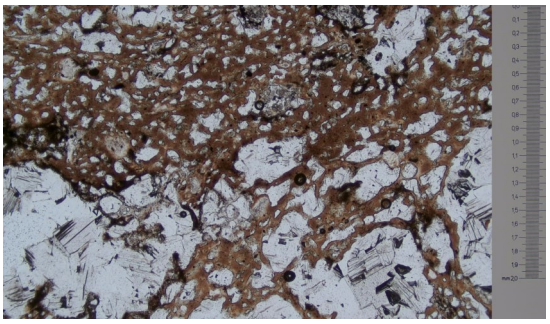

Figure 14. Photo in PPL, taken at 4x magnification. The image shows an example of how regularly spaced the clasts inside of the melt are (melt in brown in PPL), indicating melting in place. Other than melting, little can be seen of shock-metamorphic features.

5.3. Sample 3B

The sample is light brown in surface colour, and the sample as a whole consists of roughly 40% brown glass (fig. 15). The rest of the sample consists of lithic clasts which measure below a centimetre in size. Flow channels can also be easily recognized by the absence of clasts.

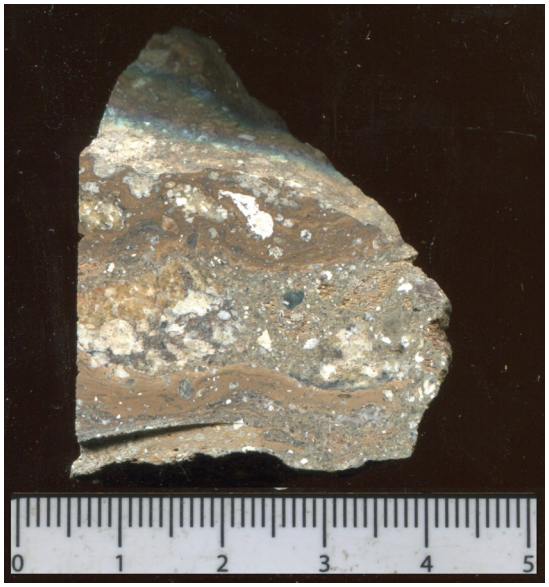

Figure 15. Photo of sample 3B in hand sample post cutting.

Thin section 3BB

It's mineral content is dominated by quartz and feldspar, and with biotite being a minor component. The quartz is generally found in recrystallized aggregates and often contains PDFs. All estimated 40% of the sample consists of orange to dark-brown glass and all of it is devitrified. Within glassy regions of the thin section, coronas of aluminium silicate are common around altered grains, and vesicles are present in some areas within the glassy parts. A crack with seemingly unaffected quartz and feldspar is present in the sample (fig. 16).

No BSE or EDS was done on thin section 3BB.

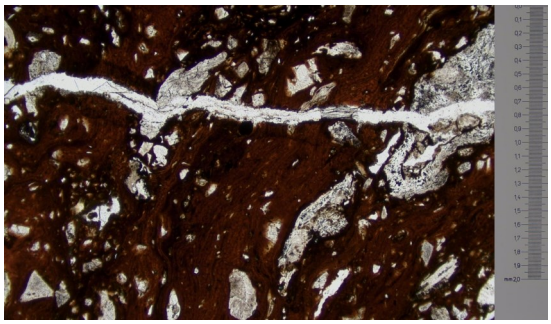

Figure 16. Photo in PPL, at 4x magnification. The image shows the dark brown glass of thin section 3BB which contains numerous angular clasts and an infilled secondary crack which appears whiter than everything else and passes through the entire thin section, left to right in the image. Flow textures are easily seen in the glass, and the minerals contained in the clasts (mostly feldspar and quartz) are highly altered.

5.4. Sample 3C

The sample has a thinner and less fragile outside layer than either 1A or 3A (fig. 17). There are also no vesicles which can be seen by the naked eye. Black melt can be seen forming channels. The melt is found throughout the sample, but is concentrated in the channel regions. lithic clasts generally appear clearly as they consist mostly of white feldspar. Two thin sections were made from sample 3C (Thin sections 3CA and 3CH).

Thin section 3CH

3CH features an estimated 70% black glass, 10% dark brown glass and 20% crystalline material (fig. 18). Acicular feldspar microlites are found throughout the glass, which is in contrast to most other samples examined from the area. The dark brown glass is well preserved, showing less signs of devitrification than glasses in the other samples. Mineralogically, quartz and feldspar dominate, with biotite being a minor component. all the feldspar is highly altered, and PDFs are com-

Figure 17. Sample 3C in hand sample.

mon in quartz crystals. An estimated 50% of all quartz has also been recrystallized and is found as recrystallized aggregates which do not contain PDFs. Nearly all quartz which is not part of these aggregates contain PDFs and are toasted. In plane polarized light, flow textures in the glass are apparent.

Thin section 3CH was found to contain multiple types of shock-metamorphic features in magnetite and apatite. In magnetite, multiple grains were found to have undergone dynamic recrystallization (fig. 19). The apatite of 3CH was also found to have turned granular and had formed possible vesicles (fig. 20). The vesicles are found close to the centres of the apatite grains, while the outer parts of the grains have turned granular. The centres of the apatites in 3CH appear nearly unaffected while the outer layers of the grains were turned granular. One example of apatite had dissociated and scattered into the surrounding melt in all visible directions (fig. 21).

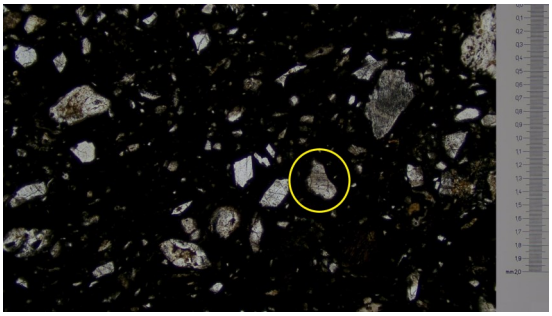

Figure 18. An overview photo taken at 4x amplification of thin section 3CH. Lithic clasts are contained in a pitch black matrix of devitrified black glass. A grain of quartz displaying PDFs is circled, while most other grains in view are partially melted and highly altered rather than containing PDFs.

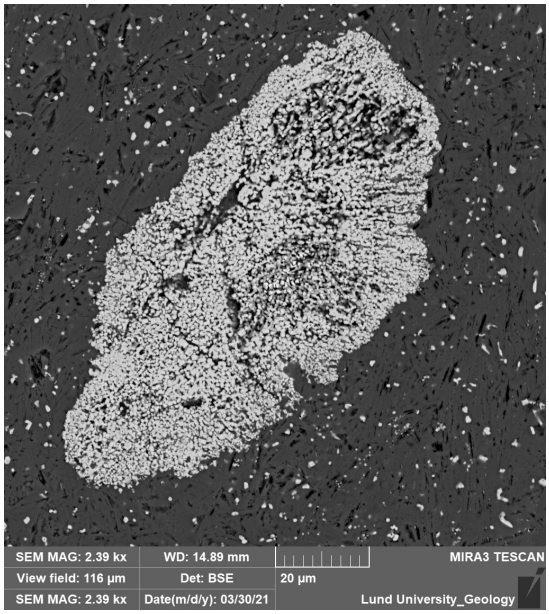

Figure 19. A magnetite grain from thin section 3CH which has turned granular, and one of the most highly recrystallized examples of magnetite in this study.

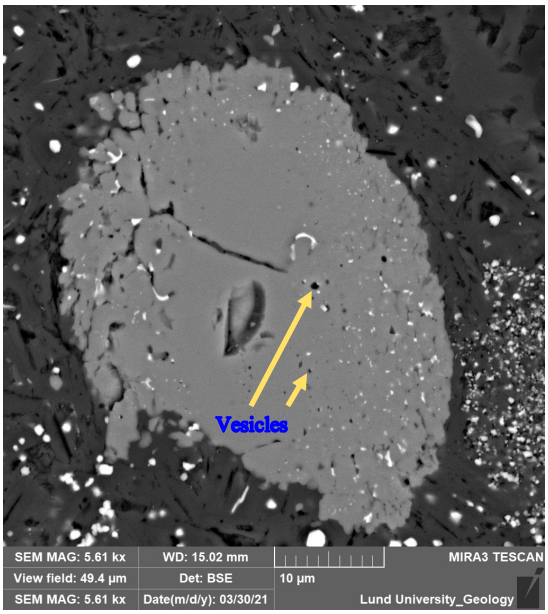

Figure 20. An apatite grain from thin section 3CH seen in BSE, which displays granularity and possible vesicles. The grain also seems to have a fracture running through its centre. The centre of the grain appears largely unaffected by the shock, while the outer parts have undergone shock-metamorphism.

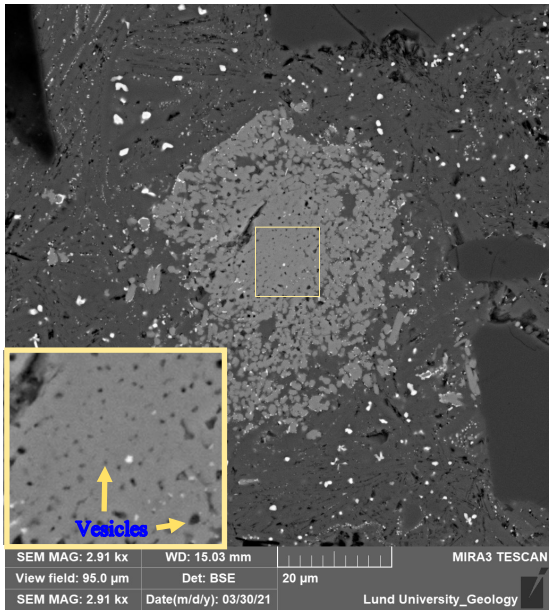

Figure 21. An apatite grain (coloured light grey) seen in BSE, displaying what appears to be vesicles (small black dots in its centre which gradually increase in size with distance from the centre) in its central parts. The grain has also dissociated and scattered in all visible directions into the surrounding devitrified glass.

Thin section 3CA

thin section 3CA shares the same chemistry characteristics as Thin section 3CH, since they were taken from the same sample. Heavily altered and extremely fine-grained mineral aggregates in a dark brown devitrified glass matrix. It is mostly full of recrystallized quartz aggregates as well as glass which may constitute lechatelierite (fig. 22), as well as with heavily altered feldspars.

No SEM analysis was carried out on thin section 3CA.

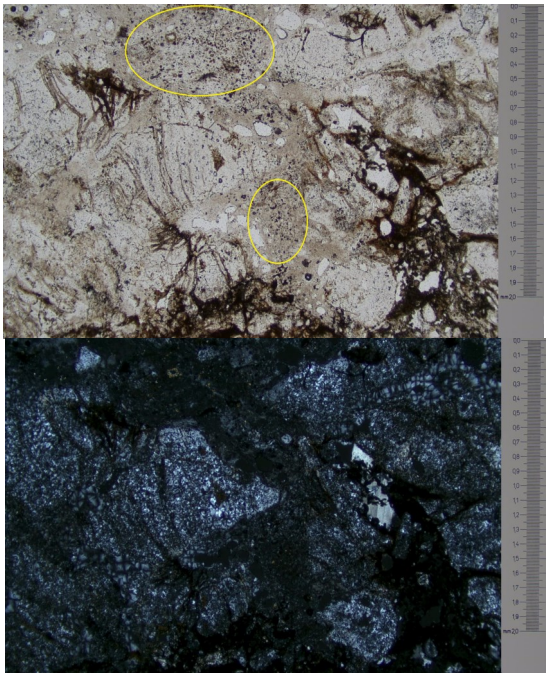

Figure 22. Photograph of thin section 3CA taken at 4x magnification in PPL. Some areas suspected to be lechatelierite due to the texture of vesicles or inclusions are circled in yellow. Dark brown areas are glass, while parts coloured light brown is diaplectic quartz glass, being nearly completely extinct in XPL.

5.5. Sample 3S

The outside surface of the sample is dark grey in colour, and there is barely any perceptible weathering surface which differs in physical properties from the inside, except in colour (fig. 23). The matrix inside is mostly grey and brown in some parts and consists of devitrified glass. small lithic fragments can be seen and appear white in colour.

Thin section 3SC

The quartz of this thin section is commonly recrystallized into aggregates in melted zones, and spherulite/axiolite are common throughout the melted areas of the thin section. Quartz and feldspar dominate while biotite, ilmenite, aluminium silicates (in coronas) and magnetite are minor constituents. PDFs are common in quartz, kink bands are found in some biotite (fig, 24) and the feldspar is generally highly altered (fig. 25).

Figure 23. Sample 3S in hand sample.

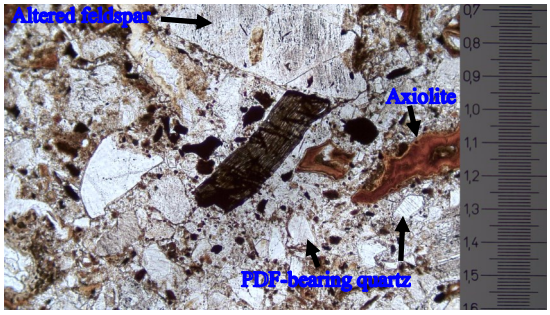

Figure 24. Photo taken in PPL at 10x magnification in thin section 3SC of a biotite grain which contains kink bands. Surrounding the biotite grain are opaque phases in black, glass in brown nuances and multiple grains of quartz containing PDFs as well as altered feldspar grains which appear “dusty”. In the brown melt areas, thin axiolite can be observed in the interface between the melt and the surrounding crystals (appearing in a light brown colour).

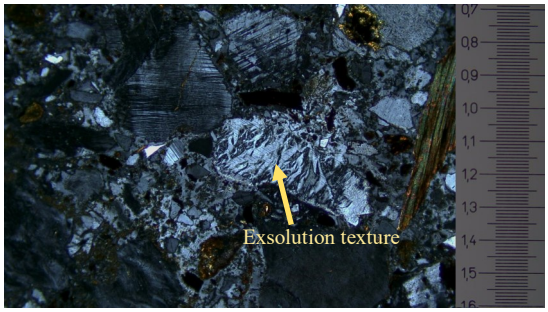

Figure 25. Photo of Thin section 3SC at 10x magnification in XPL. In the centre, a feldspar grain can be seen containing exsolution textures. Surrounding it are k-feldspars with linear features, a few “dusty”-looking altered feldspar grains and a biotite grain in a matrix of small quartz crystals and glass.

There are two types of devitrified glass in this sample. A light brown and a much darker brown glass. Aluminium silicate coronas are nearly omnipresent in melt-crystal interfaces of the light brown glass, but completely absent in the darker brown glass.

Thin section 3SC was found to contain apatite which has experienced dynamic recrystallization (fig. 26), and contain vesicles.

A recrystallized magnetite grain was also found containing apparently continuous, linear or planar features (fig. 27). This magnetite grain is not nearly as porous as some other recrystallized magnetite grains. A zircon grain was found to have dynamically recrystallized and partially metamorphosed into baddeleyite (fig. 28).

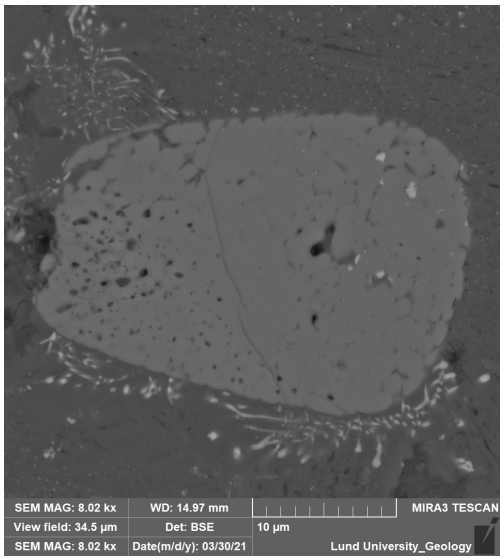

Figure 26. BSE image of an apatite from thin section 3SC. The apatite has turned nearly completely granular. In the left hand side of the grain, the granular texture is less obvious, and a high frequency of black spots indicate a different texture than the right side.

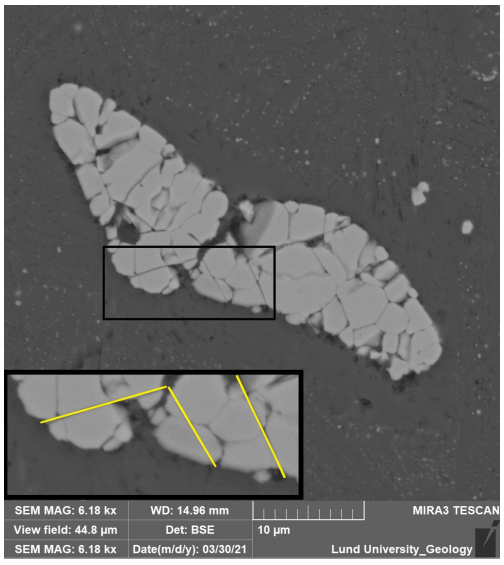

Figure 27. A recrystallized iron oxide grain from thin section 3SC which contains continuous linear features (marked in yellow).

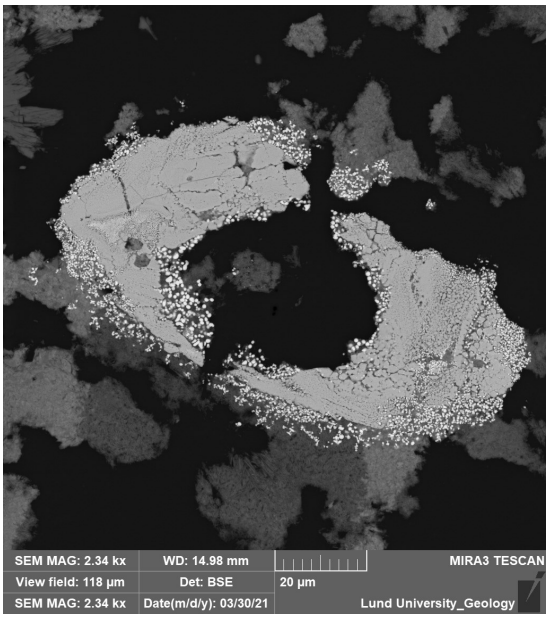

Figure 28. BSE image of A recrystallized Zircon ($ZrSiO_4$) from thin section 3SC. It is surrounded by aggregates of baddeleyite (ZrO_2), a polymorph of zircon.

Figure 29. Sample 3T in hand sample.

5.6. Sample 3T

The sample has a dark grey colour both on the outside and inside, but appears slightly lighter in colour on the outside due to wear which is likely a result of grinding against other rocks in the water (fig. 29).

Thin section 3TA

This thin section features a higher melt/crystal ratio than most of the samples, estimated to consist of 70% devitrified dark chocolate-coloured brown glass. Microlites form quenching textures in glassy parts. Larger, more well-developed crystals are found in contact with grains which have not melted. The mineral content consists of mostly quartz, plagioclase, k-feldspar and minor

biotite. Aluminium silicate coronas surround most crystals (fig. 30), and axiolite/spherulite is also found in small amounts. Recrystallized quartz aggregates are common, as are quartz crystals with PDFs (fig. 31). It is also very common for quartz grains containing PDFs to be toasted in this sample. In PPL, flow-textures become very apparent. Some feldspar has also turned diaplectic. This sample is the only one in which titanite was found to have been clearly affected, displaying exsolution textures.

Among apatite grains found in the sample, only one was found to have partially undergone dynamic recrystallization (fig. 32), while multiple magnetite grains were found to also have turned granular (fig. 33, 34). One magnetite grain also seems to have experienced some annealing (fig. 35). Zircon was also found to have dynamically recrystallized and to have metamorphosed into baddeleyite (fig. 36). Two titanite grains were found with exsolution textures and possible vesicles (fig. 37). These are the only instances of these features in titanite which were found throughout all the samples.

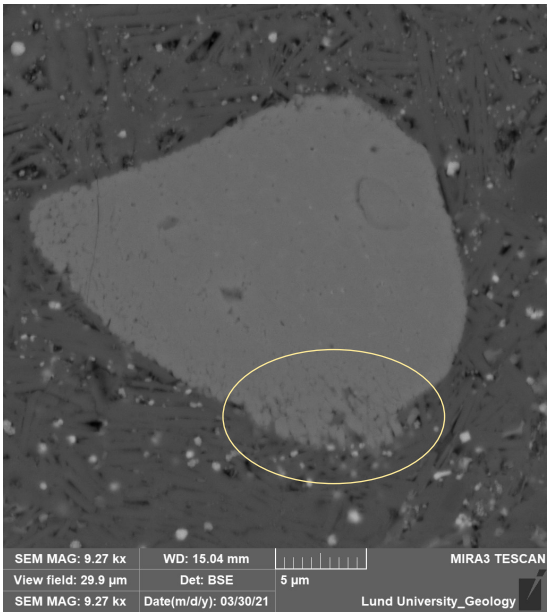

Figure 32. A partly granular apatite found in thin section 3TA. Though it is hard to see, the grain is completely recrystallized. The aggregate has mostly kept the shape of the original grain. A small portion in the bottom part of the grain has broken out of the shape of the original grain, circled in yellow.

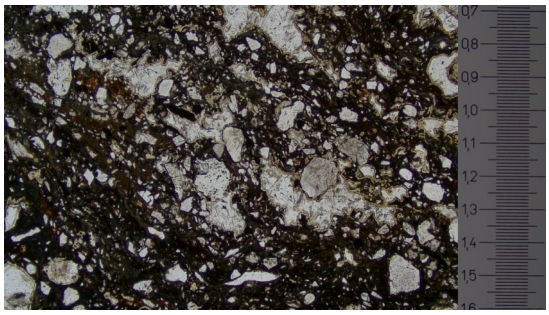

Figure 30. Photo taken in PPL of thin section 3TA at 4x magnification. Mineral grains in white are mostly quartz and feldspar grains. Surrounding nearly all grains are yellow-coloured thin coronas of aluminium silicate or axiolite in some cases.

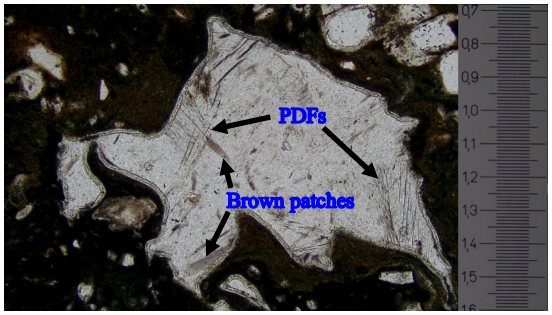

Figure 31. Photo from thin section 3TA, taken in PPL at 10x magnification. A partially melted quartz grain with PDFs, some of which are "open". The grain also has a thin corona which results from the devitrification of the surrounding pitch black glass. In addition, the grain displays brown patches of unknown origin.

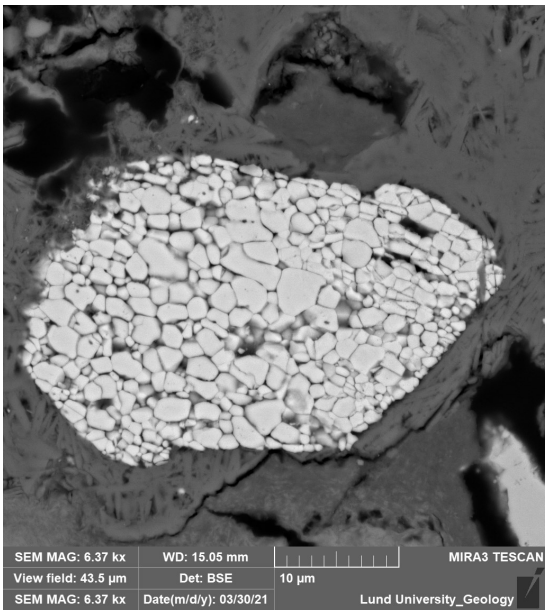

Figure 33. A magnetite grain from sample 3TA which has tuned granular. In contrast to most other recrystallized magnetite grains, each sub-grain appears nearly pristine. Little sign of neither fracturing, partial recrystallization or annealing in the sub-grains.

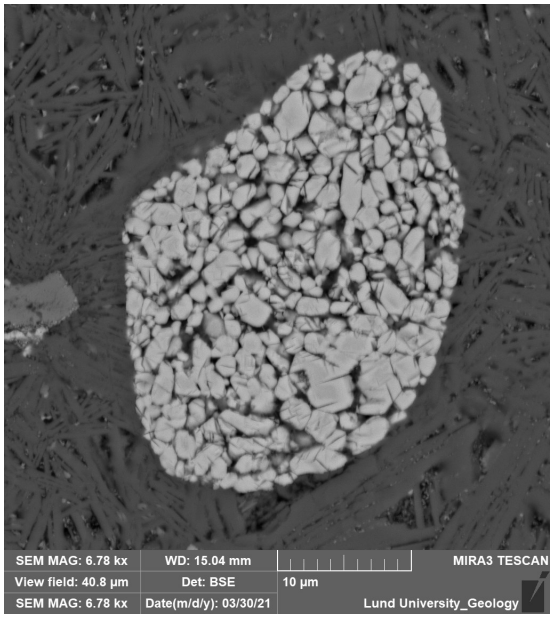

Figure 34. Another magnetite grain turned granular from thin section 3TA. In this case, the sub-grains seem to have cracked or partially recrystallized in nearly every sub-grain.

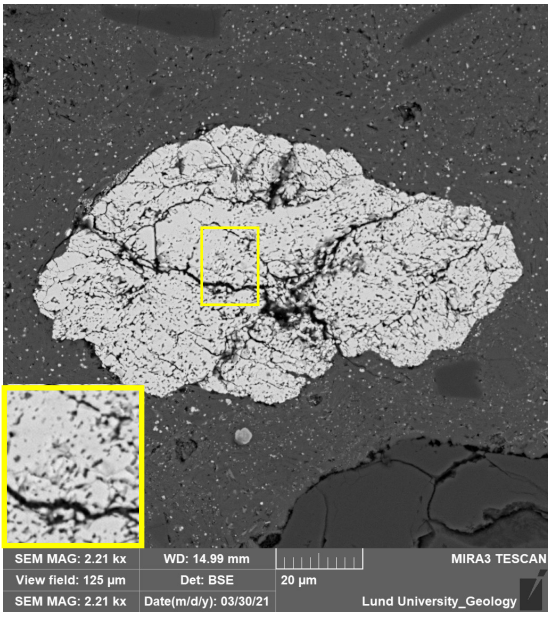

Figure 35. BSE image of an amorphous magnetite grain from thin section 3TA which has recrystallized. The sub-grains may have partially annealed.

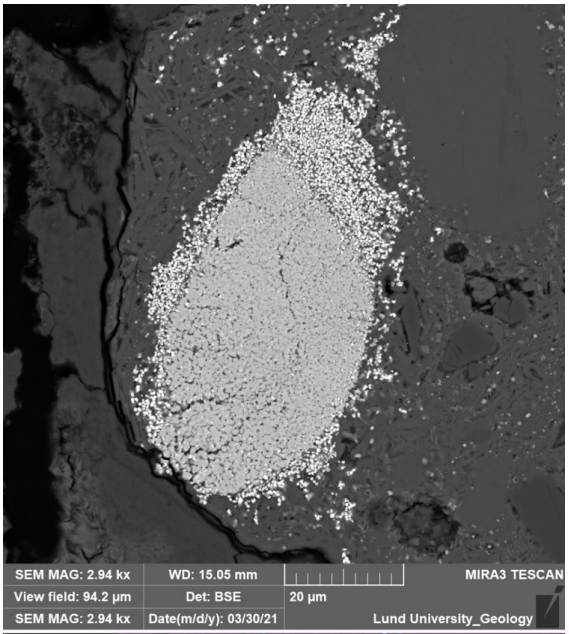

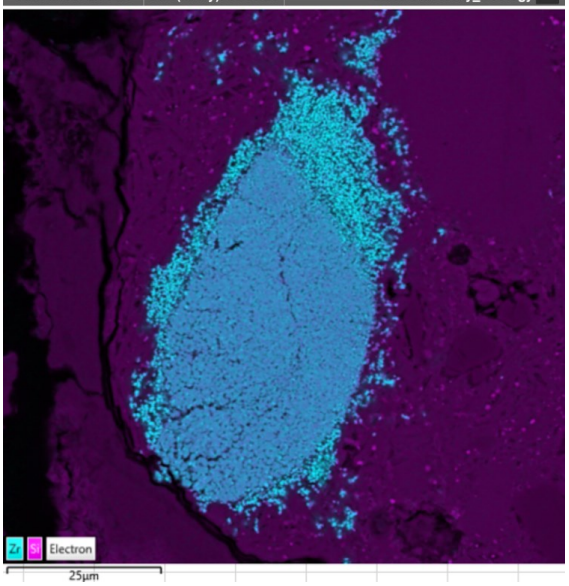

Figure 36. A zircon grain from thin section 3TA, in BSE on top and EDS on bottom. The grain has turned completely granular, and the outer layers of the crystal have formed baddeleyite, which has a higher concentration of zirconium than zircon does.

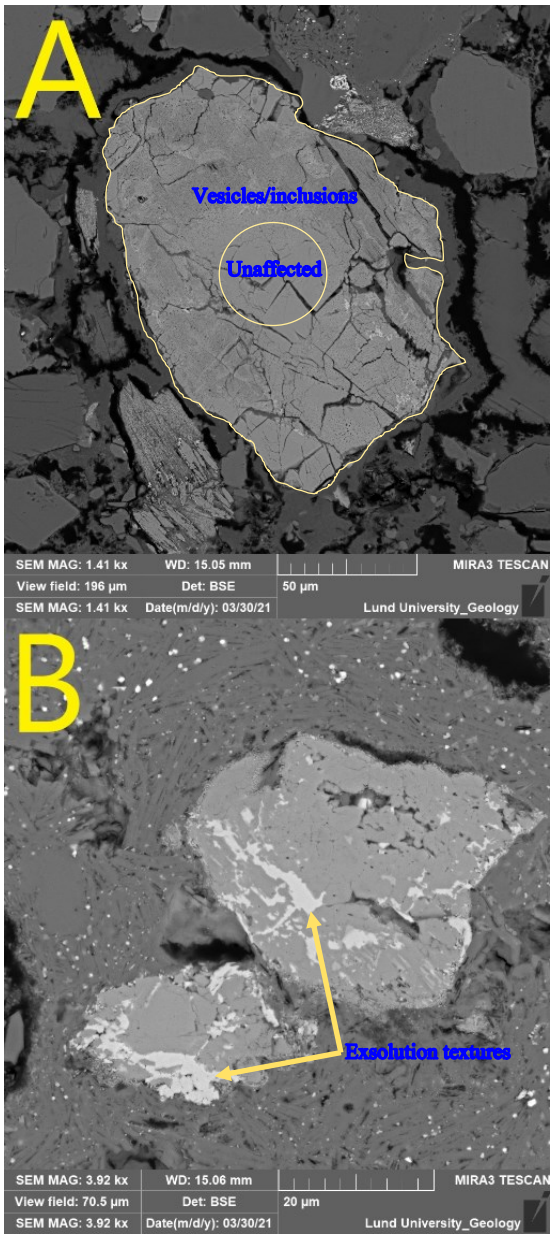

Figure 37. Titanite grains in a devitrified glass matrix from thin section 3TA, viewed in BSE. Both grains display intragranular exsolution textures in white. A) Highly fractured grain which seems to have a gradient of effects increasing outward from the centre. The central parts of the grain appear unaffected, while the more peripheral parts are rich in micro-vesicles or inclusions, appearing matte and darker grey in colour. near fractures, the vesicles are absent in some places. B) Two titanite grains which might have been one previously. These grains have clearer exsolution textures than the previous image, but no micro-vesicles/ inclusions are present. The upper grain has recrystallized into an aggregate of sub-grains.

5.7. Sample 3Y

The large central lithic clast can be seen in white, as well as many surrounding smaller fragments in a matrix of brown and grey glass (fig. 38). The sample has barely any signs of withering on the outside other than scraping from other rocks.

Figure 38. Photo of sample 3Y in hand sample. The-Central clast is visible in light brown and white colors.

Figure 39. Photo of thin section 3YB, Taken in XPL at 10x magnification. A quartz and feldspar aggregate viewed in XPL at 10x magnification. In the right hand side of the image, dozens of spherulites displaying "Maltese crosses" can be seen. In the centre of the image, there is also a zone of unusual recrystallization or fracturing of unclear origin (circled yellow).

Thin section 3YB

A fully crystalline feldspar and quartz aggregate in the middle of the thin section is surrounded by devitrified glass. The edges of the clast are partially melted and consist of orange to dark-brown glass. The edges are also surrounded by axiolite all around the large central clast, but not farther away from the clast. The ratio of glass to crystals increases with distance from the central clast. Flow textures are apparent on the basis of directional alignment of clasts within the melt. Edges of the central clast has extensive patches of spherulite (fig. 39) and ballen textures are found in some of the edges of larger sized grains in the sample (fig. 40).

No BSE, EDS or EBSD was performed on thin section 3YB.

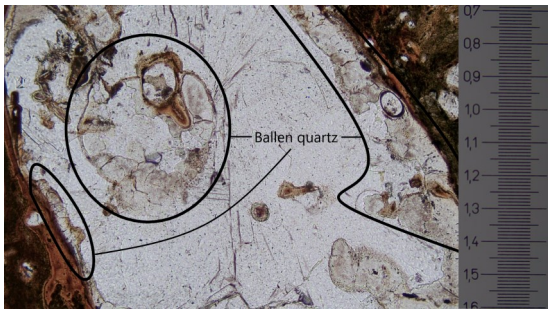

Figure 40. Example of ballen quartz texture from thin section 3YB, circled in black.

5.8. Sample 5B

The sample appears dark grey both on the outside and on the inside (fig. 41). The inside appears in a slightly darker grey than the outside, much like all other samples. Again, due to the scraping against other rocks. On the inside, glass dominates, with two centimeter-sized clasts and many millimeter-sized clasts in it. The sample is also somewhat fragile, as it was found with a half developed crack in it.

Thin section 5BC

This thin section features two distinct colours of devitrified glasses. One is light brown and another which is dark brown in colour. The total fraction of glass is estimated to be 30%. Compositionally, it is very similar to all other samples, containing mostly quartz and feldspar with minor biotite. As far as shock-metamorphic features, it contains Toasted quartz with PDFs and ballen quartz. The glass features very small (around 1-5 micrometre) round iron oxide grains throughout the glass. These iron oxide grains form non-coherent "clouds" especially around partially melted biotite, but also around quartz. Aluminium silicate coronas are common around all types of grains (fig. 42).

Figure 41. Sample 5B in hand sample.

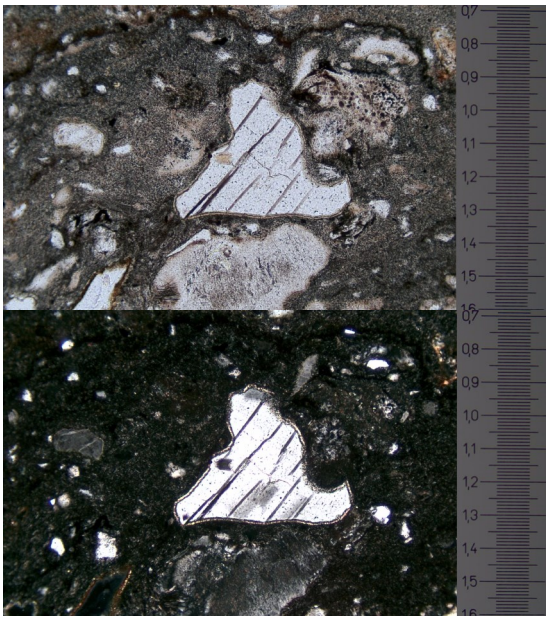

Figure 42. Photos in PPL on top and XPL on bottom, taken at 10x magnification. Unrecognized mineral which contains linear features of unclear origin and tiny inclusions which appear as black dots. The grain is also surrounded by a corona of aluminium silicate and is completely surrounded by devitrified glass, but does not seem to have reacted much to the shock wave in the way of recrystallizing.

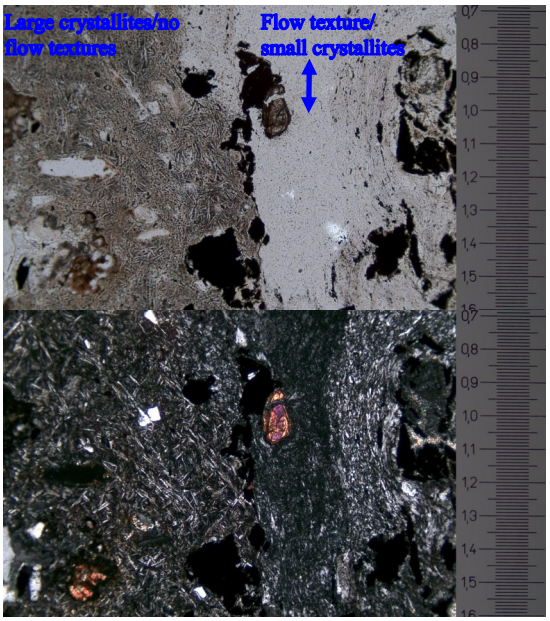

Figure 43. Photos in PPL on top and XPL on bottom, taken at 10x magnification. Almost everything in the photo is devitrified glass, but there are two distinctly different textures. One consists of relatively large crystallites which do not seem to have any signs of flow textures, while the other has extremely small crystallites and a clear direction of flow in the direction top-bottom. This is also confirmed by the directional alignment of the few small crystals that are present.

One grain of unknown mineral type was found with lamellae that do not change in colour in PPL or go extinct upon rotation in XPL (fig. 42). The glass in the thin section is composed mostly of acicular feldspar crystals and quartz grains (fig. 43) just a handful of micrometers in length each, but in parts the individual microlites of the devitrified glass are larger than in any of the other thin sections.

No BSE or EDS analysis was done on thin section 5BC.

6. Discussion

6.1. Sample classification

The samples are estimated to vary between about 20-70% melt, but all contain a mixture of shocked and unshocked clasts of material of varying sizes, mixed in with light brown to pitch black glass, often in the same sample (5BC, 3SC and 3BB all have brown and black glass which have not mixed). The high fraction of melted material across all samples lead to the classification of all samples as 'suevitic impact melt breccias' (Stöffler, 2018).

All samples are felsic in composition, containing high amounts of silica in all cases, with some local variations. According to proposals in Stöffler (2018) on the systematic classification of impactites, the first letter of the classification for all samples is as such "F".

Following this letter is a number corresponding to the degree of shock-metamorphism the sample experienced, denoted S1- S7 where S1 means unshocked and S5-S7 means whole-rock melting. All samples in this study varies between S2-S4, as no samples are unshocked, and no samples exhibit whole-rock melting. The specific classification for each individual sample will be noted below.

6.2. Samples 1A, 3A and 3B

Out of these samples, only thin section 1AA was examined using the SEM. Because few signs of shock-metamorphic features beyond PDFs were found in the polarizing microscope studies, it's unlikely for any of these samples to contain additional features.

There are some textures in melted areas of sample 3B, namely areas rich in vesicles, which may be lechatelierite. If it is indeed lechatelierite, then that would indicate a high magnitude of shock exposure, but the uncertainty is deemed high enough that it will be disregarded.

Samples 1A and 3A were the only samples which were found to contain vesicles visible to the naked eye, showing that there was at least one volatile present. Interestingly, they also experienced the weakest shock among the samples which was an unexpected correlation. Based on the findings, excluding the suspected lechatelierite, they are all classified as F-S2.

6.3. Sample 3C

Since two thin sections were made from sample 3C, and the two samples feature quite different ratios of melt/crystalline material and findings of shock-metamorphic features, a single classification is given for the sample as a whole. Based on the granitic composition and tentative findings of lechatelierite and highly recrystallized magnetite among other features, and the relatively high degree of melt, the sample is believed to have been close to whole-rock melting. Therefore the sample as a whole is classified as F-S4.

Thin section 3CH

BSE and EDS revealed recrystallized magnetite and apatite in thin sample 3CH. Recrystallization of magnetite has been shown to occur between 20 and 30 GPa, while little is known about shock reactions in apatite.

Of particular interest are two apatite grains. The first is a partially recrystallized grain which contains vesicles or inclusions (fig. 20). If these black "dots" inside of the crystals are indeed vesicles, that might indicate that there was indeed some degassing of the apatite (likely releasing Chlorine, Fluorine and water.

The second apatite (fig. 21) displays multidirectional scattering. The central parts of the grain (which are most intact) also seem to contain vesicles.

Given that apatite is a potential source for a variety of volatiles (Adcock, 2017; Moser *et al, 2020*), it may be that the volatiles which are trapped inside the crystal exert tensile stress upon the crystal, possibly assisting the multidirectional dissociation. Currently, it is thought that degassing occurs after decompression (Langenhorst, 2002).

The recrystallized magnetite grains found have recrystallized into sub-grains which are roughly one micrometre across in size. This was also the case for most of the highly recrystallized magnetite grains found in all of the thin sections during the study.

Thin section 3CA

All quartz and feldspar grains in the thin section are highly rounded and/or amorphous. In general, the quartz has recrystallized. There is a possibility that parts of the quartz glass is lechatelierite (fig. 22). The formation of lechatelierite in granite requires shock magnitudes of 72,5-85 GPa (Schrand & Deutsch, 1998), which would be close to the whole-rock melting point and the highest shock magnitude among the samples studied. Though lechatelierite is difficult to conclusively identify, if it is diaplectic glass, it still requires 22-80 GPa to form (Stöffler et al, 1986; Sharp et al, 1999; Chen & El Goresy, 2000; Kubo et al, 2010; El Goresy et al, 2013).

A feature which was not seen in other samples, was the apparent cracking of the glass matrix due to volume expansion of constituent mineral grains. This thin section was never analysed in

the SEM.

Judged collectively, thin sections 3CH and 3CA are classified as F-S4

6.4. Sample 3S

Thin section 3SC

The features found indicate that shock pressures were likely not as high as those found in 3CH. No highly recrystallized magnetite grains were found, which likely indicates pressures below 30 GPa (Kontny, 2018). One magnetite grain was found which seemed to be recrystallized in a more orderly form than grains found in other samples (fig. 27) and containing linear features. These linear features are interpreted to be twins (Alwmark *et al*, 2022).

Other features found were recrystallized zircon, baddeleyite formation and fully recrystallized apatite with black spots tentatively identified as vesicles (fig. 26), but which may constitute inclusions. This might indicate that the recrystallization of zircon and apatite, and degassing of apatite occurs below 30 GPa as well.

Based on these findings of multiple types of shock-metamorphic features requiring medium to high magnitudes of shock and the amount of crystalline material remaining, the sample is classified as F-S3.

6.5. Sample 3T

Thin section 3TA

This sample had the highest number of types of shock-metamorphic features found in it. They include quartz PDFs, recrystallized apatite, zircon transformation to baddeleyite, titanite exsolution textures and recrystallized magnetite. Additionally, an image of a magnetite grain (fig. 35) shows a different texture. It's believed that the unusual appearance relative to other grains could be due to annealing post-shocking (Reznik *et al*, 2016, Kontny *et al*, 2018). The features found in the titanite of this thin section, as well as the possible annealing of the magnetite, were only found in this thin section. However, only one recrystallized apatite grain (fig. 32) was found among many unaffected grains (unaffected grains in appendix figures 10, 11, 12 and 13). In the case of the titanite exsolution textures, it is unclear whether the feature is shock-related.

A comparative feature between samples is how many recrystallized magnetite grains were found relative to apatites. In sample 3T the number of recrystallized magnetite grains found is higher than the number of apatites. The reverse was true in sample 3S. The reason for the discrepancy is likely purely statistical in nature, but one might also speculate that it could be related to how shock waves refract in different mediums, seeing as the two minerals have vastly different densities. Perhaps the density of the minerals relative to the surrounding melt/matrix plays a role in which mineral is more heavily affected by the shock wave.

The classification for sample 3T is F-S3, based on the wide suite of shock-metamorphic features found, and the amount of melt. The absence of lechatelierite might indicate that the sample would have needed a higher magnitude of shock for whole-rock melting to occur.

6.6. Sample 3Y

Thin section 3YB

On the basis of finding ballen quartz, it is believed that the sample was exposed to temperatures $\geq 1200°C$ and 35 GPa at least (Ferriere *et al,* 2009). Since ballen quartz does not have a single definitive precursor mineral, a precise pressure figure is difficult to pinpoint. It is suggested to form out of a variety of shock-induced states which all require high shock-pressures and/or temperatures, including diaplectic glasses, cristobalite and lechatelierite (Ferrière *et al*, 2010).

The thin section features a relatively large central clast, which due to its vastly different constituent grainsizes (relative to its surroundings) and rounded edges has been interpreted to be partially melted. There is also a visible gradient in grain sizes scaling down as distance increases from the central grain, and a lot of spherulite. On the basis of the high amount of spherulite, the sample likely represents a relatively cold xenoclast which was carried along in the hot melt until it cooled enough that it crystallized completely.

Spherulites nucleate at temperatures close to crystallization, and would have nucleated right before the whole melt crystallized (Lofgren, 1971). The high concentration of spherulites in certain areas of the sample result in some of them creating angular interfaces between each spherulite. Although not important in the context of shock-metamorphism, it may be of interest to those interested in nucleation and crystallization granitic rocks like this.

Based on the findings of ballen quartz and high fraction of melt and overlooking the tentative xenoclast and lack of PDFs within it, the classification is F-S3.

6.7. Sample 5B

Thin section 5BC

The glass matrix in this sample consists of larger crystals than in any of the other samples, potentially indicating to either a slower quenching (meaning a longer time for chemical reactions to occur before it gets too cold, thus leading to larger crystals) or higher degree of devitrification.

The sample also contains ballen quartz which again indicates $\geq 1200°C$ and 35 GPa at a minimum. In addition, the high degree of alteration in feldspars and recrystallization of quartz likely means a high magnitude of shock exposure, but since no SEM studies were performed on this sample, no additional shock-metamorphic features can be confirmed to be present.

Based on the findings of ballen quartz and otherwise extensive metamorphic effects and melt-

ing, the sample is classified as F-S3.

6.8. Reflections on shock-metamorphic features in apatite and magnetite

Four recrystallized apatites were found to have undergone dynamic recrystallization, and all apatites which recrystallized, did so into sub-grains which range in size between roughly 5-10 -µm across.

No chemical anomalies could be discerned in the granular apatite grains relative to the ones which were not turned granular (see appendix figure 7), but small pores or vesicles have formed in some recrystallized parts of all grains, and generally close to the centres or less granular areas of the crystals.

Magnetite grains have frequently undergone dynamic recrystallization (e.g. figures 19, 33, 34, 35). The recrystallized magnetite grains found have recrystallized into sub-grains which are roughly one micrometre across in size. This was the case for most of the highly recrystallized magnetite grains found in all of the thin sections during the study.

Additionally, in one instance the sub-grains in such a recrystallized aggregate may have started annealing, as well as taking on an amorphous shape (fig. 35). It is interpreted that the unusual appearance relative to other grains could be due to annealing.

The annealing behaviour in magnetite may also be a reason for the high magnetic readings present in the central uplift structure in Dellen (Liu *et al*, 2008; Kontny *et al*, 2018, Reznik *et al, 2016*). Further, the implication may be that these magnetic readings can be used to determine a temperature zone within Dellen where the temperature post-impact exceeded the 973 K required for annealing and resultant magnetic property recovery to occur (Kontny *et al*, 2018).

Another feature found in magnetite were possible twins or alternately, well-developed fractures (fig. 27) that appear perfectly linear. Twinning has previously been experimentally shown to be caused by shock exposure of magnetite above 10 GPa (Reznik *et al*, 2016). These linear features translate across sub-grains, which might indicate that the feature developed before the recrystallization was completed.

6.9. Glass characteristics

The variability in colour of the glass seems to affect chiefly the type of coronas which envelop much of the lithic fragments within the melt. In the black glass aluminium silicate coronas are common, crystallites are smaller and vesicles are also smaller as well as fewer in numbers than those found in the brown glass. Additionally, there is less porosity in the black glass.

Flow textures are common and very easily seen in the brown glass, but could only sparingly be observed in the black glasses because of the low opacity of the black glass.

The brown glass is more likely to form axiolite and spherulites.

In general, the difference between the black glasses and brown glasses is likely their chemistry, seeing as they are seemingly immiscible since they can be clearly distinguished in all samples. A characteristic of the black glass is likely a deficit in silica, based on a lack of spherulite/axiolite in the black glass compared to the brown variety.

Axiolites and spherulites (consisting of cristobalite and feldspar) are quite common throughout the samples in general. These nucleate at temperatures close to that of crystallization. Their sizes and numbers depend on the cooling rate and the amount of nucleation sites (Lofgren, 1971). They are however not associated with shock-metamorphism at all. Nonetheless, they are more common and larger in the lighter-coloured glasses than in the black glasses.

7. Conclusions

This study of rocks from the Dellen impact structure, Sweden, found that apatite, magnetite, titanite and zircon all contain shock-metamorphic features. They are all interpreted to have undergone recrystallization, and apatite also displays tentative vesicles in addition to granularity. Zircon grains have partially recrystallized into baddeleyite.

EDS shows no clear sign that any of the apatite changed in its chemical composition despite both recrystallizing and displaying vesicles. However, the presence of possible vesicles and findings of signs of fracturing related to degassing highlight that apatite may well release volatiles during or shortly following impacts.

All samples represent suevitic impact breccias, and only the least shocked (1A and 3A, which likely experienced 10-20 GPa) contained vesicles clearly visible to the naked eye. The highly shocked samples also contained vesicles, but these were only visible in the glass phases under a microscope.

Out of the four thin sections which were analysed using SEM techniques, The magnetite was found to have recrystallized in all samples but 1A, indicating that in the relatively low pressure range, the recrystallization of magnetite and the resultant changes in magnetic properties should be lesser in areas which experienced relatively low shock-magnitudes since annealing of magnetite at 973 K causes annealing and magnetic property recovery (Reznik *et al, 2016)*.

The samples are classified between F-S2 and F -S4 as all felsic in composition, but display a wide range of shock-metamorphic features. None of the samples display whole-rock melting, but all contain shock-metamorphic features such as PDFs which indicate minimum shock pressures of about 10 GPa.

8. References

Adcock, C, T., Tschauner, O., Hausrath, E.M., Udry, A., Luo S.N., Cai, Y., Ren, M., Lanzirotti, A., Newville, M., Kunz, M., and Lin, C. 2017. Shock-transformation of whitlockite to merrillite and the implications for meteoritic phosphate. *Nature Communications* 8. Article number 14667.

Alvarez, L.W., Alvarez, W., Asaro, F., Michel, H.V. 1980. Extraterrestrial Cause for the Cretaceous-Tertiary Extinction. Science, Volume 208, issue 4448.

Alwmark, S. 2016. Terrestrial consequences of hypervelocity impact – Shock metamorphism, shock barometry, and newly discovered impact structures. Lund University, Faculty of Science, Department of Geology, Lithosphere and Biosphere Science.

Alwmark, S., Erickson, T.M., Cavosie, A.J. Empirical constraints on progressive shock metamorphism of magnetite from the Siljan impact structure, Sweden. Geology. Volume 3, Issue 50. Pp 377-382.

Baier, J. 1901. Geohistorische Bemerkunger zur Suevit-Forschung (Ries-Impakt). Geohistorische Blätter, 31(1/2).

Bland, P.A., Artemieva, N.A. 2003. Efficient disruption of small asteroids by Earth's atmosphere. Nature. Volume 424, issue 6946, Pp 288-291.

Boynton, W.V. 1984. Chapter 3: Cosmochemistry of the Rare Earth Elements: Meteorite Studies. Developments in Geochemistry. Volume 1-2, issue 52, Pp 63-114.

Bunch, T.E, Cohen A.J., Dence, M.R. 1967. Natural Terrestrial Maskelynite. American Mineralogist. Volume 1-2, issue 52, Pp 244-253.

Burbine, T.H., McCoy, T.J., Meibom, A., Gladman, B., Keil, K. 2002. Meteoritic Parent Bodies: Their Number and Identification. Asteroids III. University of Arizona Press.

Burton, A.S., Elsila, J.E., Hein, J.E., Glavin, D.P., Dworkin, J.P. 2013. Extra-terrestrial amino acids identified in metal-rich CH and CB carbonaceous chondrites from Antarctica. Meteoritics and Planetary Science. Volume 48, issue 3, Pp 390-402.

Cavosie, A.J., Lugo Centeno, C. 2014. Shocked Apatite from the Santa Fe Impact Structure (USA): A New Accessory Mineral for Studies of Shock Metamorphism. 45th Lunar and Planetary Science Conference, held 17-21 March, 2014 at The Woodlands, Texas. LPI Contribution No. 1777. Pp.1691.

Chen, M., El Goresy, A. 2000. The nature of maskelynite in shocked meteorites: Not diaplectic glass but a glass quenched from shock-induced dense melt at high pressures. Earth and Planetary Science Letters. Issue 179, Pp 489–502.

El Goresy, A., Gillet, P., Miyahara, M., Ohtani, E., Ozawa, S., Beck, P., Montagnac, G. 2013. Shock-induced deformation of Shergottites: Shock-pressures and perturbations of magmatic ages on Mars. Geochimica et Cosmochimica Acta. Issue 101, Pp 233– 262.

Engelhardt, W.V. 1972. Shock produced rock glasses from the Ries crater. Contributions to Mineralogy and Petrology. Issue 36, Pp 265-292.

Erickson, T.M., Kirkland, C.L., Timms, N.E., Cavosie, A.J., Davison, T.M. 2020. Precise radiometric age establishes Yarrabubba, Western Australia, as Earth's oldest recognised meteorite impact structure. Nature Communications. Issue 11, Article number 300. doi: 10.1038/s41467-019-13985-7.

European Space Agency. Retrieved march 3rd, 2021. "what is the difference between asteroids and comets?" Rosetta's frequently asked questions.

Ferrière, L., Koeberl, C., Libowitzky, E., Reimold, W.U., Greshake, A. 2010. Ballen quartz and cristobalite in impactites: New investigations. Geological Society of America Special Papers. Issue 465, Pp 609-618.

Ferrière, L., Koeberl, C., Reimold, W.U. 2009. Characterisation of ballen quartz and cristobalite in impact breccias: new observations and constraints on ballen formation. European Journal of Mineralogy. Volume 21, Issue 1, Pp 203-217.

Ferriére, L., Koeberl, C., Reimold, W.U., Libowitzky, E., Greshake, A. 2008. Ballen quartz and cristobalite in impact breccias: types, occurrence, and possible origin. Large Meteorite Impacts and Planetary Evolution IV. Volume 1423, Pp 3011.

Filiberto, J., Treiman, A.H. 2009. Martian magmas contained abundant chlorine, but little water. Geology. Issue 37, Pp 1087-1090.

French, B. M., Short, N.M. 1968a. Shock metamorphism as a geological process. Mono Book Corp., Baltimore. Shock Metamorphism of Natural Materials. Pp. 1–17.

French, B. M. 1969. Distribution of shock-metamorphic features in the Sudbury Basin, Ontario, Canada. Meteoritics. issue 4, Pp 173–174.

French B. M. 1990b. 25 years of the impact-volcanic controversy: Is there anything new under the sun or inside the Earth? AGU. Eos, volume 71, issue 17, Pp 411-414.

French, B.M. 1998. Traces of Catastrophe: A Handbook of Shock-Metamorphic Effects in Terrestrial Impact Structures. LPI Contribution No. 954, Lunar and Planetary Institute, Houston. 120 Pp.

Fritz, J., Fernandes, V.A., Greshake, A., Holzwarth, A., Böttger, U. 2019. On the formation of diaplectic glass: Shock and thermal experiments with plagioclase of different chemical compositions. Meteorics & Planetary Science. Volume 54, Issue 7, Pp 1533-1547.

Gault, D.E., Collins, R.J., Gold, T., Green, J., Kuiper, G.P., Masursky, H., O'Keefe, J., Phinney, R. Shoemaker E.M. 1968. Lunar Theory and Processes. Journal of Geophysical Research. Volume 73, Issue 12, Pp 4115-4131.

Gault, D.E., Wedekind J.A. 1969. The destruction of tektites by micrometeoroid impact. Journal of Geophysical Research. Volume 74, Issue 27, Pp 6780-6794.

Grieve, R.A.F., Pilkington, M. 1996. The signature of terrestrial impacts. Reviews of Geophysics. Volume 30, issue 2, Pp 161-181.

Goldstein, J. 2003. Scanning Electron Microscopy and X-Ray Microanalysis. Springer. ISBN 978-0-306-47292-3.

Goltrant, O., Leroux, H., Doukhan, J., Cordier, P. 1992. Formation mechanisms of planar deformation features in naturally shocked quartz. Physics of Earth and Planetary Interiors. Volume 74, issues 3-4, Pp 219 -240.

Halls, H. 1979. The Slate Islands meteorite impact site: a study of shock remanent magnetization. Geophysical Journal International. Royal astronomical society. Volume 59, Pp 553-559.

Kenny, G.G., Karlsson, A., Schmieder, M., Whitehouse, M.J., Nemchin, A.A., Bellucci, J.J. 2020. Recrystallization and chemical changes in apatite in response to hypervelocity impact. Geology. Volume 48, issue 1, Pp 19-23.

Kontny, A., Reznik, B., Boubnov, A., Goettlicher, J., Steininger, R. 2018. Post-Shock Thermally Induced Transformations in Experimentally Shocked Magnetite. Advancing Earth and Space Sciences. DOI: 10.1002/2017GC007331.

Kowitz, A., Güldemeister, N., Reimold, W.U., Schmitt, R.T., K. Wünnemann. 2013. Diaplectic quartz glass and SiO2 melt experimentally generated at only 5 GPa shock pressure in porous sandstone: Laboratory observations and meso-scale numerical modelling. Earth and Planetary Science Letters. Volume 384, Pp 17-26.

Kubo, T., Kimura, M., Kato, T., Nishi, M., Tominaga, A., Kikegawa, T., Funakoshi, K. 2010. Plagioclase breakdown as an indicator for shock conditions of meteorites. Nature Geoscience. Issue 3, Pp:41–45.

Liu, Q., Yu, Y., Muxworthy, A.R., Roberts, A.P. 2008. Effects of internal stress on remanence intensity jumps across the Verwey transition for multi-domain magnetite. Physics of the Earth and Planetary Interiors. Volume 169, Issues 1–4, Pp 100-107.

Lofgren, G. 1971. Spherulitic textures in glassy and crystalline rocks. Journal of Geophysical Research. Volume 76, Issue 23, Pp 5635-5648.

Mark, D., Lindgren, P., Fallick A.E. 2013. A high-precision 40Ar/39Ar age for hydrated impact glass from the Dellen impact, Sweden. Geological Society London Special Publications. Volume 378, Pp 349-366.

McCubbin, F.M., Hauri. E.H., Elardo, S.M., Vander Kaaden, K.E., Wang, J., Shearer, C.K. 2012. Hydrous melting of the Martian mantle produced both depleted and enriched shergottites. Geology, issue 40, Pp. 683-686.

McGregor, M., McFarlane, R.M.C., Spray, J.G. 2018. In situ LA-ICP-MS apatite and zircon U–Pb geochronology of the Nicholson Lake impact structure, Canada: Shock and related thermal effects. Earth and Planetary Science Letters. Volume 504, Pp 185-197.

McMullan, D. 2006. Scanning electron microscopy 1928-1965. Scanning. Volume 17, issue 3. Pp 175-185.

McSween Jr, H.Y. 1999. Meteorites and Their Parent Planets Second Edition. Cambridge University Press. 299 p.

McQueen, H.J. 2003. Development of Dynamic Recrystallization Theory. Materials Science and Engineering. A. Pp 203–208.

Melosh, H.J. 1989. Impact Cratering: A Geologic Process. Oxford Monographs on Geology and Geophysics, 11.

Meteoritical Bulletin Database. Lpi.usra.edu.

Moser, D.E., Dunlop, J., Langelier, B., Douglas, J.O., Zhao, X., Cernok, A., Darling, J., White, L., Anand, M., Tait, K.T., Kizovski, T., Franchi, I. 2020. The shocking state of apatite and merrillite in shergottite Northwest Africa 5298 and extreme nanoscale chlorine isotope variability revealed by atom probe tomography. Geochimica et Cosmochimica Acta. Volume 293, issue 15. Pp 422-437.

Mroczek, R. 2014. Microscopic shock-metamorphic features in crystalline bedrock: A comparison between shocked and unshocked granite from the Siljan impact structure. Dissertations in Geology at Lund's University. Bachelor's thesis 418.

Langenhorst, F. 2002. Shock metamorphism of some minerals: Basic introduction and microstructural observations. Bulletin of the Czech Geological Survey. Volume 77, issue 4, Pp 265–282.

Osinski, G.R., Grieve, R.A.F., Bleacher, J.E., Neish, C.D., Pilles, E.A., Tornabene, L.L. 2018. Igneous rocks formed by hypervelocity impact. Journal of Volcanology and Geothermal Research. Volume 353, Pp 25-54.

Pierazzo, E. Melosh, H.J. 2000. Hydrocode modelling of oblique impacts: The fate of the projectile. Meteoritics and Planetary Science. Volume 35, Issue 1, Pp 117-130.

Pike, R. 1988. Geomorphology of impact craters on Mercury. Mercury. University of Arizona Press. Edited by F. Vilas et al. Pp 165 – 273.

Potter, R.W.K. 2015. Investigating the onset of multi-ring impact basin formation. Icarus. Volume 261, Pp 91-99.

Reznik, B., Kontny, A., Gerhards, U. 2016. Shock-induced deformation phenomena in magnetite and their consequences on magnetic properties. Advancing Earth and Space Science. Geochemistry, Geophysics, Geosystems. https://doi.org/10.1002/2016GC006338.

Schrand, C., Deutsch, A. 1998. Formation of Lechatelierite and Impact Melt Glasses in Experimentally Shocked Rocks. Lunar and Planetary Science XXIX.

Schmidt, G., Palme, H., Kratz, K. 1997. Highly siderophile elements (Re, Os, Ir, Ru, Rh, Pd, Au) in impact melts from three European impact craters (Sääksjärvi, Mien, and Dellen): Clues to the nature of the impacting bodies. Geochimica et Cosmochimica Acta. Volume 61, issue 14, Pp 2977-2987.

Sharp, T. G., El Goresy, A., Wopenka, B., Chen, M. 1999. A post-stishovite SiO2 polymorph in the meteorite Shergotty: Implications for impact events. Science. 284:1511.

Shearer, C.K., Burger, P.V., Papike, J.J., McCubbin, F.M., Bell, A.S. 2015. Crystal chemistry of merrillite from Martian meteorites: Mineralogical recorders of magmatic processes and planetary differentiation. Meteoritics & Planetary Science 50. Number 4, Pp 649-673.

Smit, J., Hertogen, J. 1980. An extraterrestrial event at the Cretaceous–Tertiary boundary. Science, volume 285, Pp 198-200.

Spudis, P. 1993. The Geology of Multi-Ring Impact Basins: The Moon and Other Planets (Cambridge Planetary Science Old). Cambridge University Press. Pp 263.

Stöffler, D. 1971. Progressive metamorphism and classification of shocked and brecciated crystalline rocks at impact craters. Journal of Geophysical Research. Volume 76, Issue 26, Pp. 5541-5551.

Stöffler, D. 1984. Glasses formed by hypervelocity impact. Journal of Non-Crystalline Solids. Volume 67, Issue 1-3, Pp 465-502.

Stöffler, D., Ostertag, R., Jammes, C., Pfannschmidt, G., Sen Gupta, P. R., Simon, S. B., Papike, J. J., and Beauchamp, R. H. 1986. Shock metamorphism and petrography of the Shergotty achondrite. Geochimica et Cosmochimica Acta. Issue 50, Pp 889–903.

Stöffler, D., Artemieva, N. A., Wünnemann, K., Reimold, W. U., Jacob, J., Hansen, B. K. & Summerson, I. a. T., 2013: Ries crater and suevite revisited—Observations and modelling Part I: Observations: Meteoritics & Planetary Science 48, 515-589. doi: 10.1111/ maps.12086.

Stöffler, D., Hamann, C., Metzler, K. 2018. Shock metamorphism of planetary silicate rocks and sediments: Proposal for an updated classification system. Meteoritics & Planetary Science. Volume 53, Issue 1, Pp 5-49.

Swedish Geological Survey, 2021. SGUs Kartvisare: Bergartskemi. https://apps.sgu.se/kartvisare/kartvisare-bergartskemi.html

Weisberg, M.K., McCoy, T.J., Krot, A.N. 2006. Systematics and Evaluation of Meteorite Classification. “In Lauretta,

Dante, S., McSween, Jr., Harold, Y. (eds.). Meteorites and the early solar system II. Foreword by Richard P. Binzel”. Tucson: University of Arizona Press. Pp 19-52.

Wittman, A., Cavosie, A.J., Timms, N.E., Ferrière, L., Raede, A., Rasmussen, C., Ross, C., Stocklig, D., Schmieder, M., Kringi, D.A., Zhao, J., Xiao, L., Morgan, J.V., Gulick, S.P.S., IODP-ICDP Expedition 364 Scientists. 2021. Shock impedance amplified impact deformation of zircon in granitic rocks from the Chicxulub impact crater. Earth and Planetary Science Letters. Volume 575.

Wright, J.T., 2017. On Distinguishing Interstellar Objects Like ‘Oumuamua’ From Products of Solar System Scattering. Research Notes of the American Astronomical Society. Volume 1, Issue 1, article id. 38.

Wood, J.A., Chondritic Meteorites and the Solar Nebula. Annual Review of Earth and Planetary Sciences. Volume 16, Pp 53-72.

Sears, D.W.G. 1998. The case for rarity of chondrules and CAI in the early solar system and some implications for astrophysical models. Astrophysical Journal Letters. Volume 498, Pp 773–778.

Svenonius, F.V. 1895 Nasafjälls zink- och silfvergrufvor i Norrbottens län. Geologiska Föreningen i Stockholm Förhandlingar. Volume 17, Issue 4, Pp 427-451.

9. Appendix

Thin section 1AA

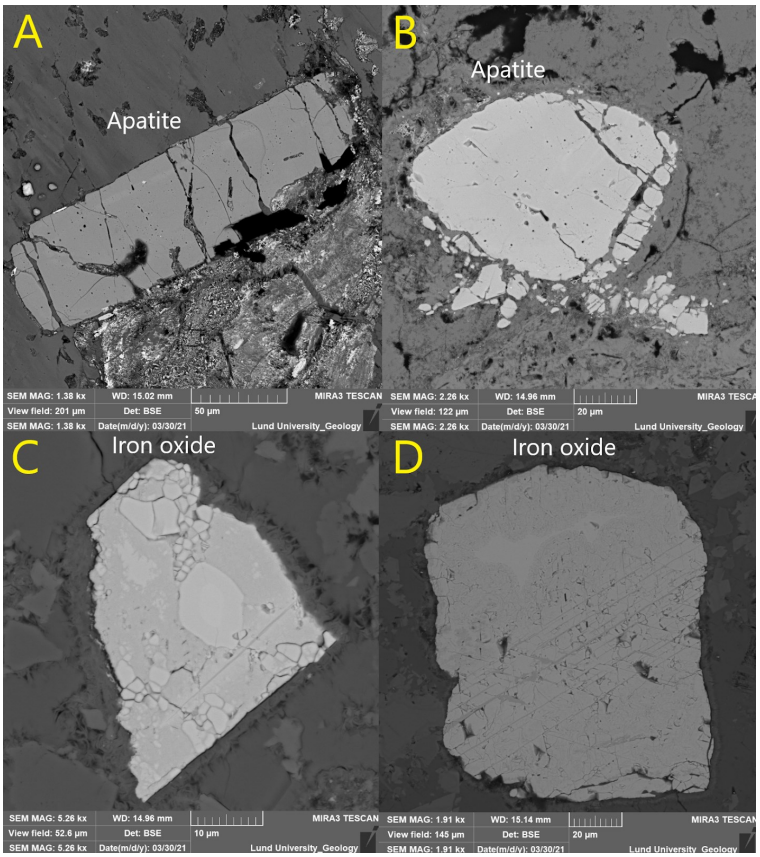

Appendix figure 1. BSE images of two unaffected apatites (A, B) and two grains of iron oxide (C, D) which are also thought to be unaffected by the shock wave. The apatites are fractured, while the iron oxides do not seem to have been fractured at all.

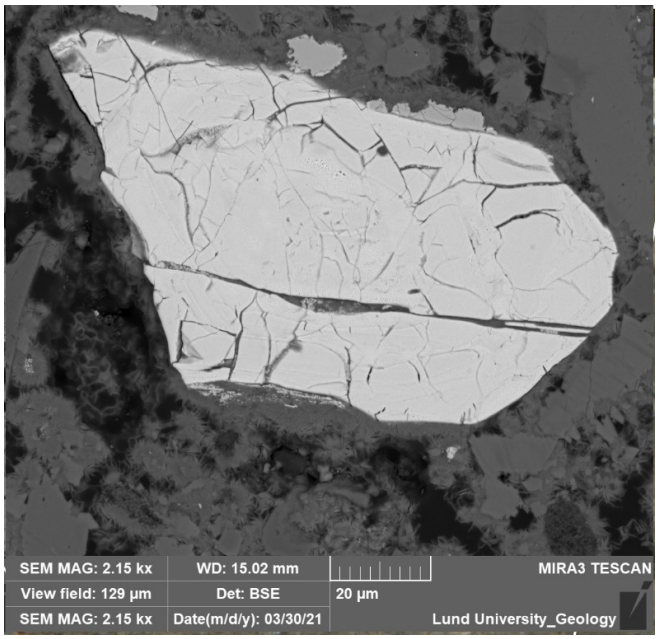

Appendix figure 2. BSE image of a fractured zircon from thin section 1AA that has not turned granular or show any other signs of metamorphic imprint. Such was also the case for all other zircons found in this thin section.

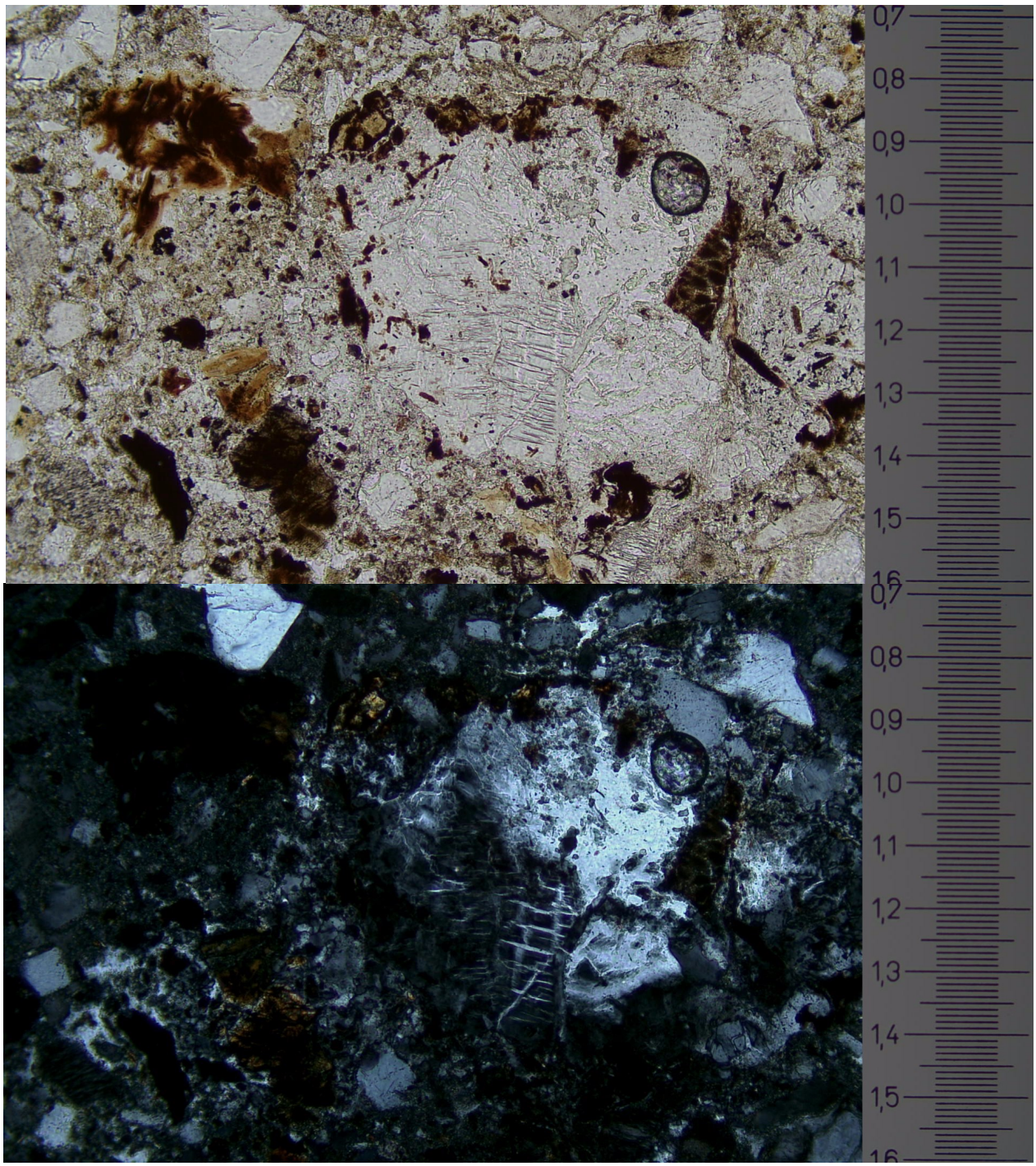

Appendix figure 3. Photos in PPL on top, and XPL on bottom. A heavily altered feldspar crystal with exsolution textures is in the centre. In PPL, the exsolved phase can be seen to have a slight green hue.

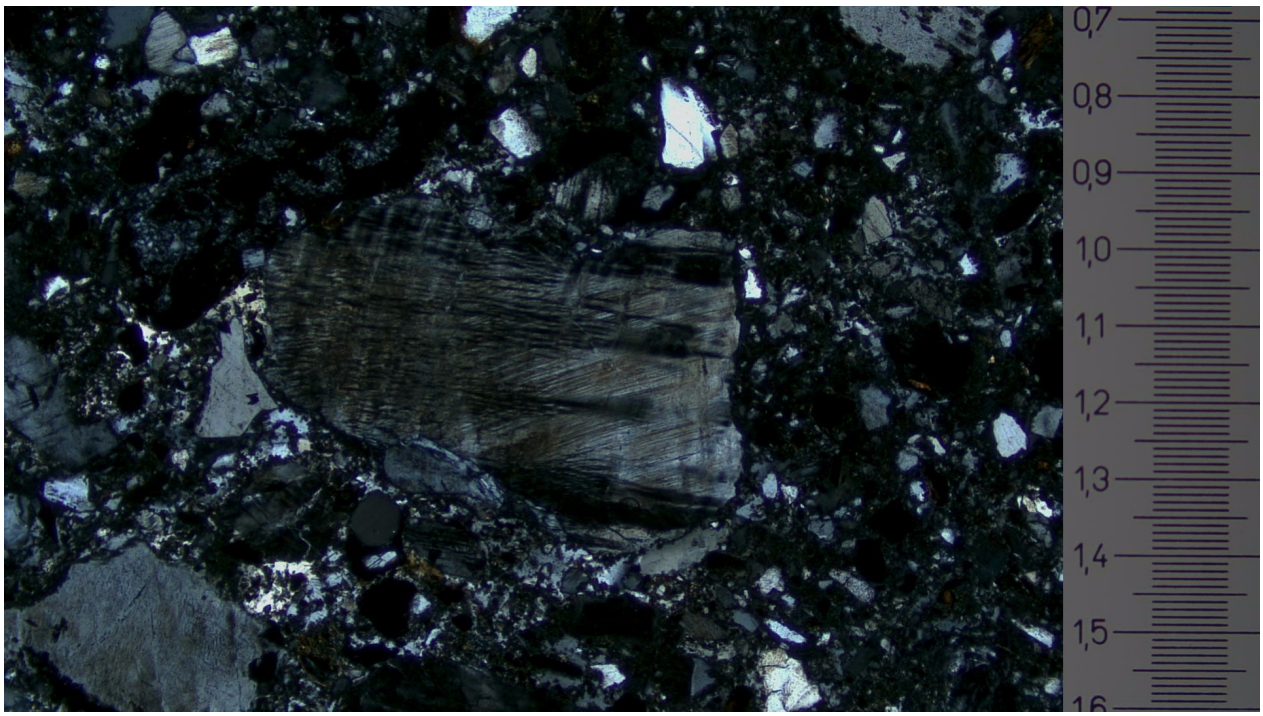

Appendix figure 4. Photo in XPL. The image shows what is believed to be a K-feldspar with PDFs.

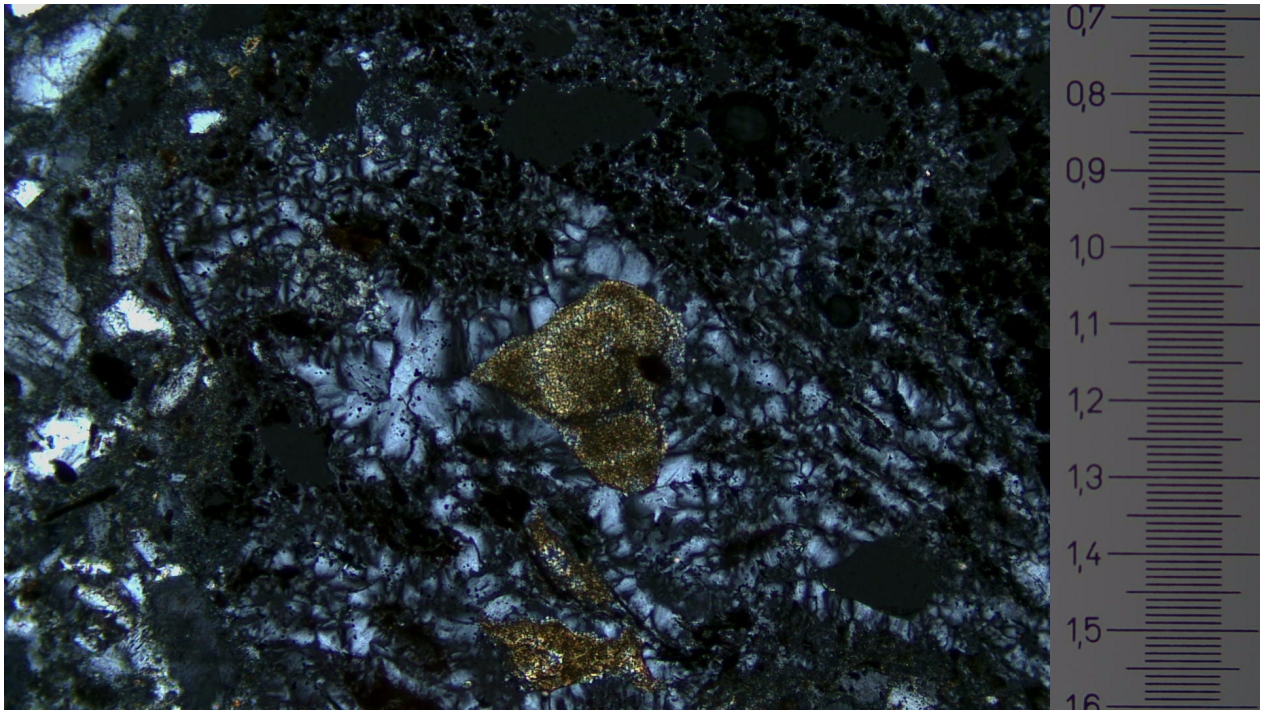

Appendix figure 5. Photo in XPL of an unknown brown/yellow mineral in the centre which seems to have been turned granular, and is displaying some kind of zoning. Surrounding it, is what is thought to be axiolite and devitrified glass.

Thin section 3CH

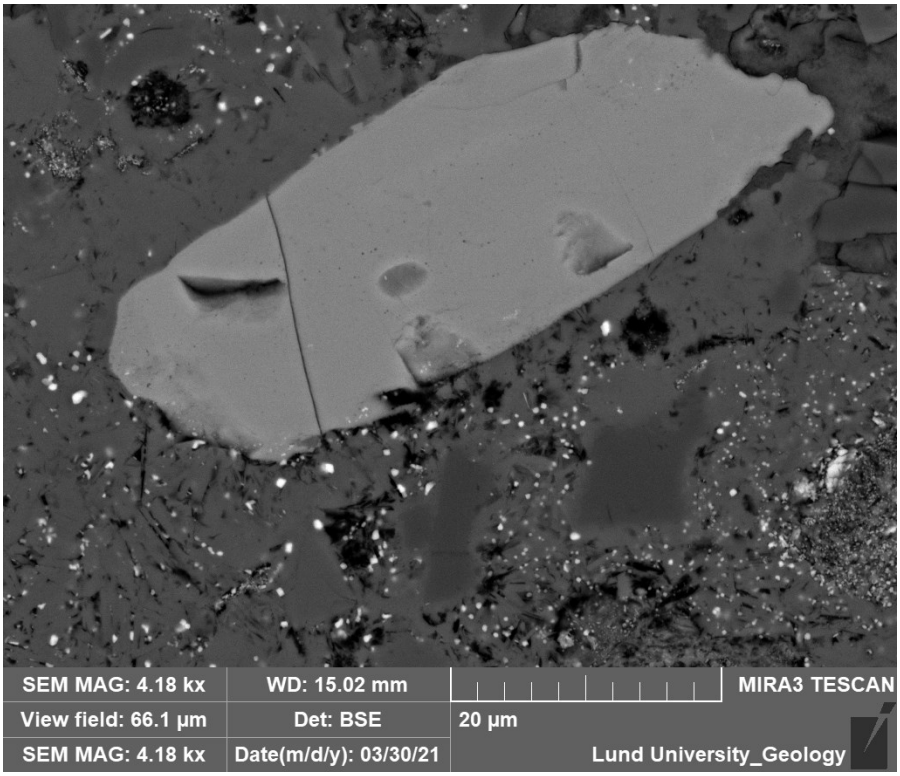

Appendix figure 6. BSE image of an apatite from thin section 3CH. The apatite has fractured, but does not show any signs of having turned granular or otherwise having been affected by the shock wave.

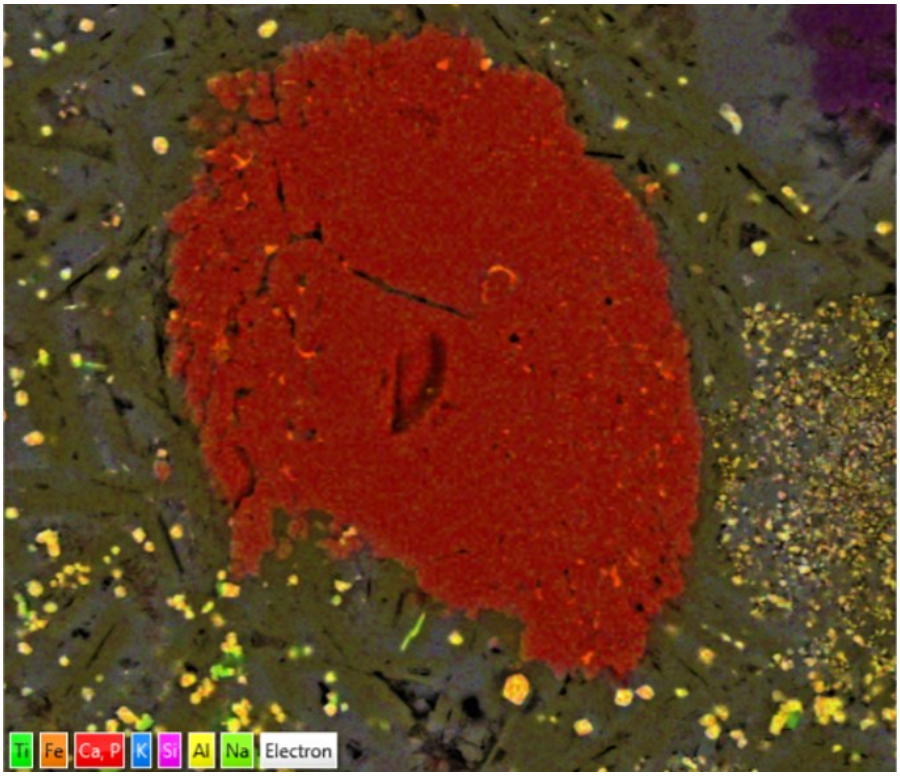

Appendix figure 7. EDS image of an apatite turned granular by the shock wave, from thin section 3CH. The crystal has a homogeneous composition. The small white spots inside of the crystal are magnetite grains.

Thin section 3CA

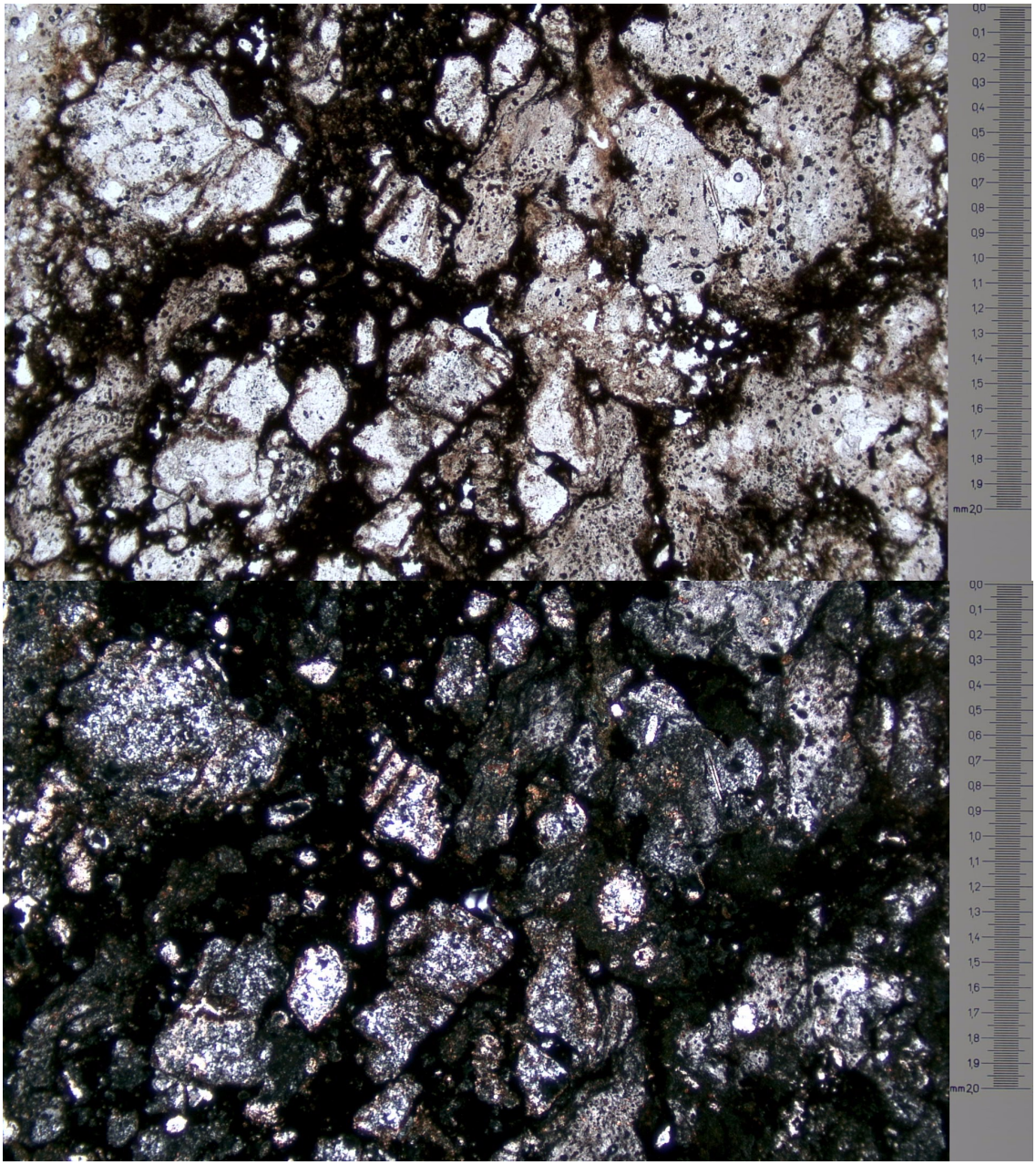

Appendix figure 8. Photos in PPL on top and XPL on bottom taken at 4x magnification in thin section 3CH. Most of the image is highly recrystallized quartz agglomerates which are believed to constitute lechatelierite, while some of the image is also altered feldspar, which are both contained in a matrix of black glass.

Appendix figure 9. Photo in XPL at 10x magnification. In the centre is a feldspar crystal which seems to have PDFs or some other kind of feature which looks like “scratches” in the centre of the crystal. Surrounding it are other altered feldspar crystals in a devitrified glass matrix.

Thin section 3SC

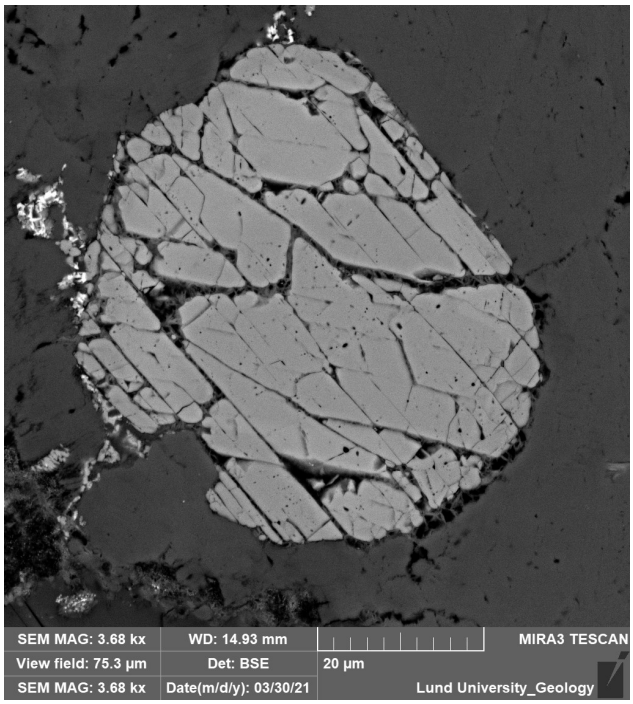

Appendix figure 10. BSE image of an apatite in thin section 3SC. It is highly fractured , but shows no granularity. It contains black spots which may be vesicles, and might indicate that the crystal was degassed to some degree.

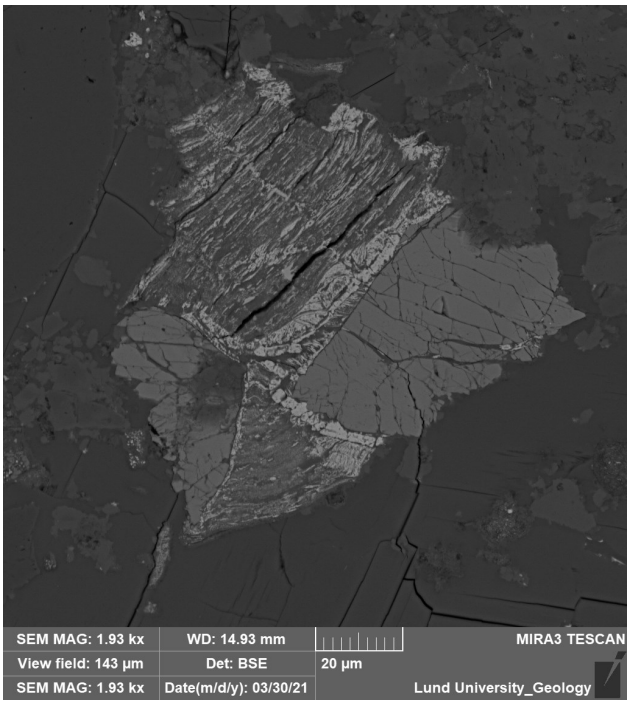

Appendix figure 11. BSE image of a heavily fractured apatite crystal in thin section 3SC which seems to have been partially metamorphosed, displaying exsolution textures the whitest regions.

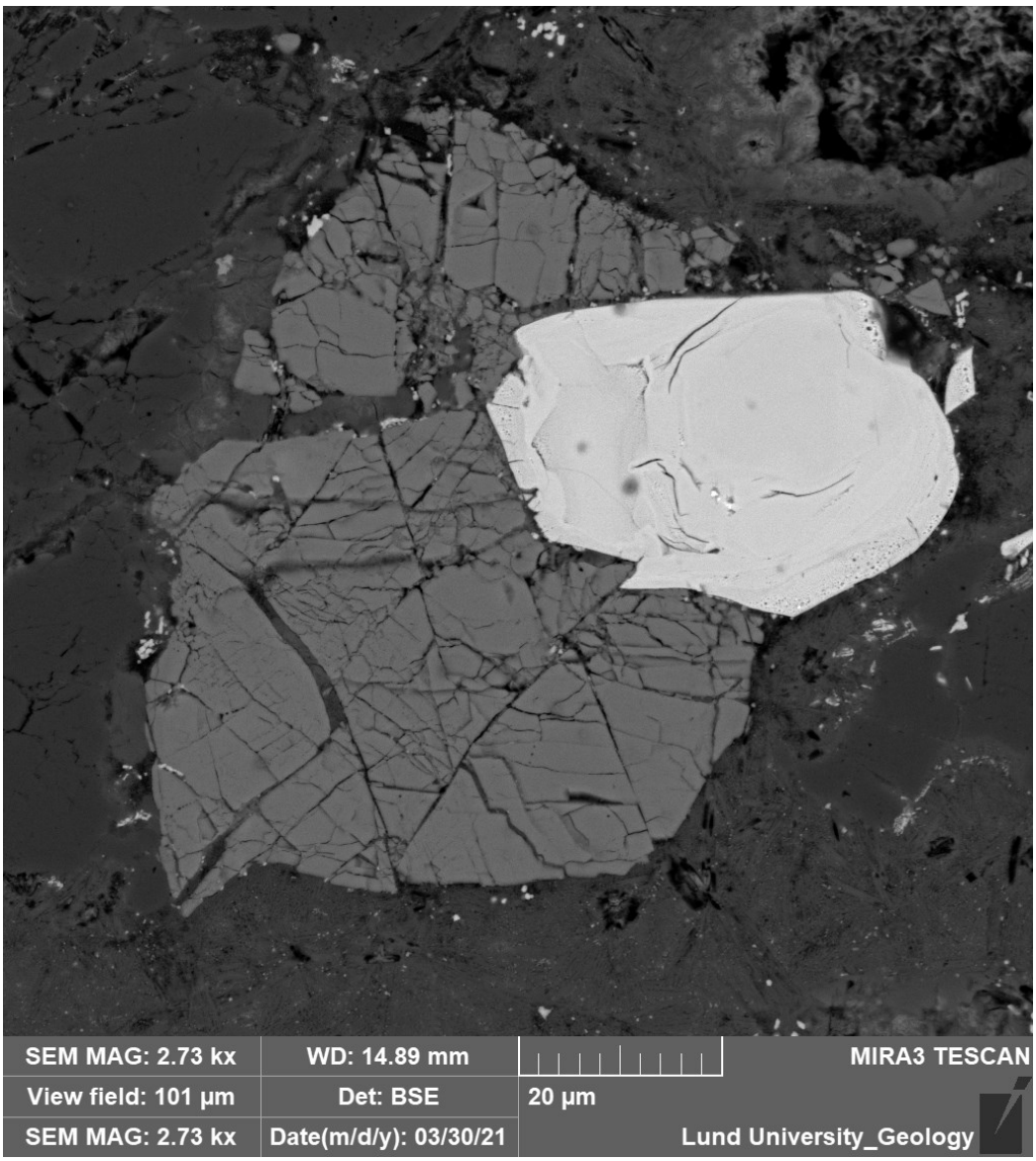

Appendix figure 12. BSE image from thin section 3SC of intergrown apatite in dark grey and zircon in white. The apatite is fractured, but otherwise unaffected by the shock wave. The zircon is displaying some kind of unknown circular feature in its centre as well as weakly visible zoning.

Thin section 3TA

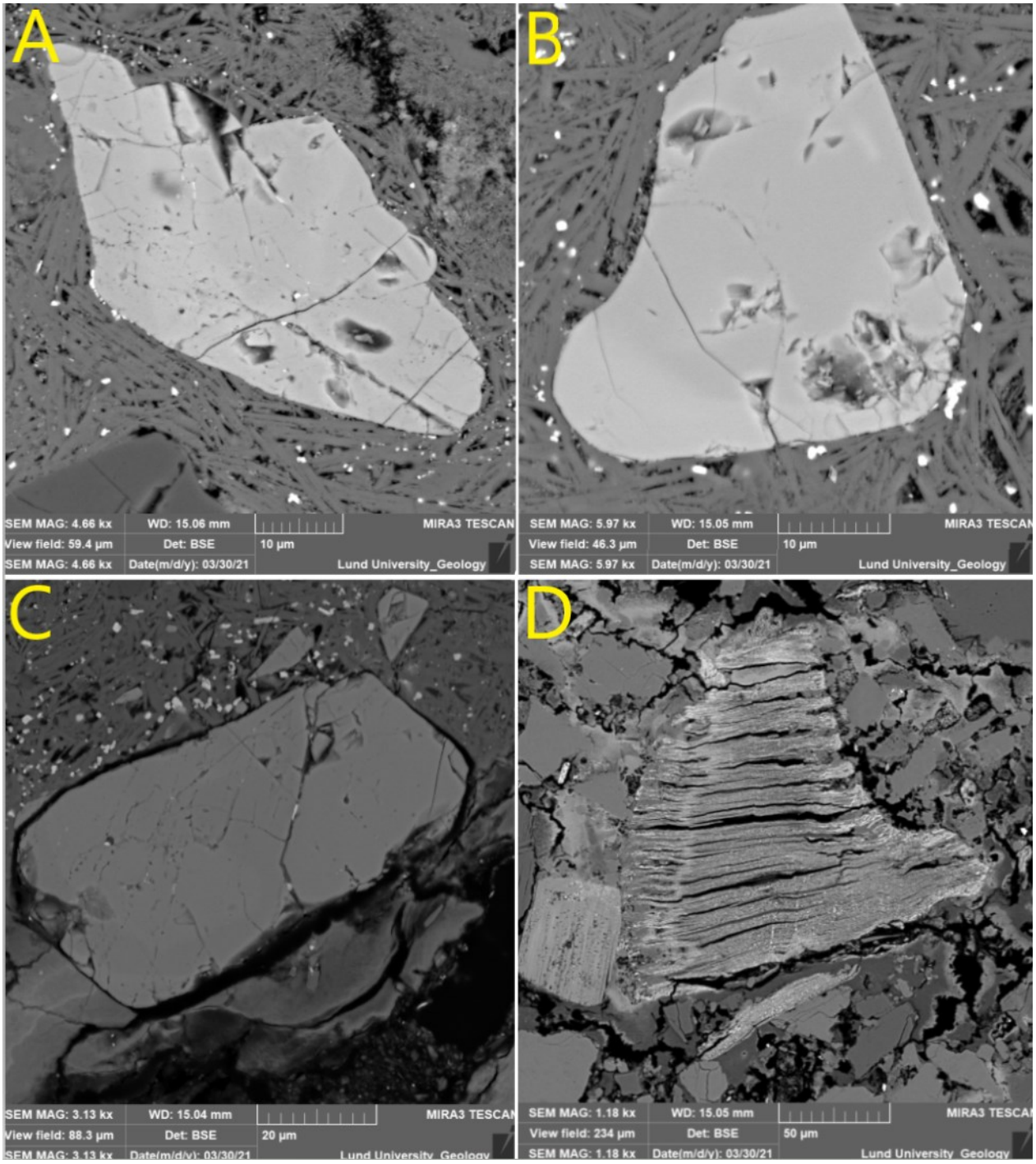

Appendix figure 13. a collection of BSE images from thin section 3TA. images A, B and C are of apatites which do not seem to have been appreciably affected by the shock waves, save for fracturing. Image D has captured a heavily altered and fractured biotite which seems to have exsolution textures, defined by white colours along edges of the grain as well as along a line in the left side of the grain.

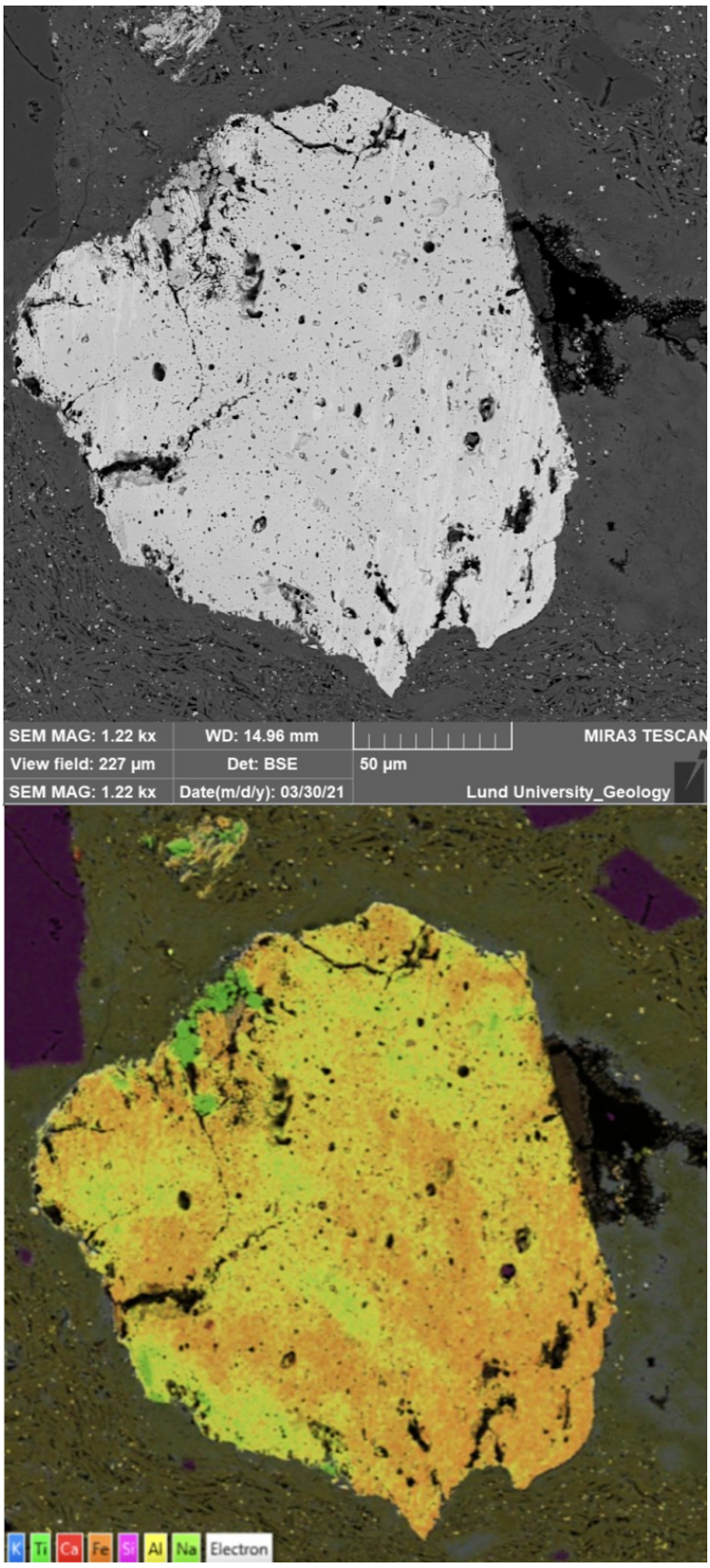

Appendix figure 14. BSE image of an iron oxide on top and EDS image on bottom. The grain has no signs of turning granular, and the EDS shows little variation of note.

Thin section 3YB

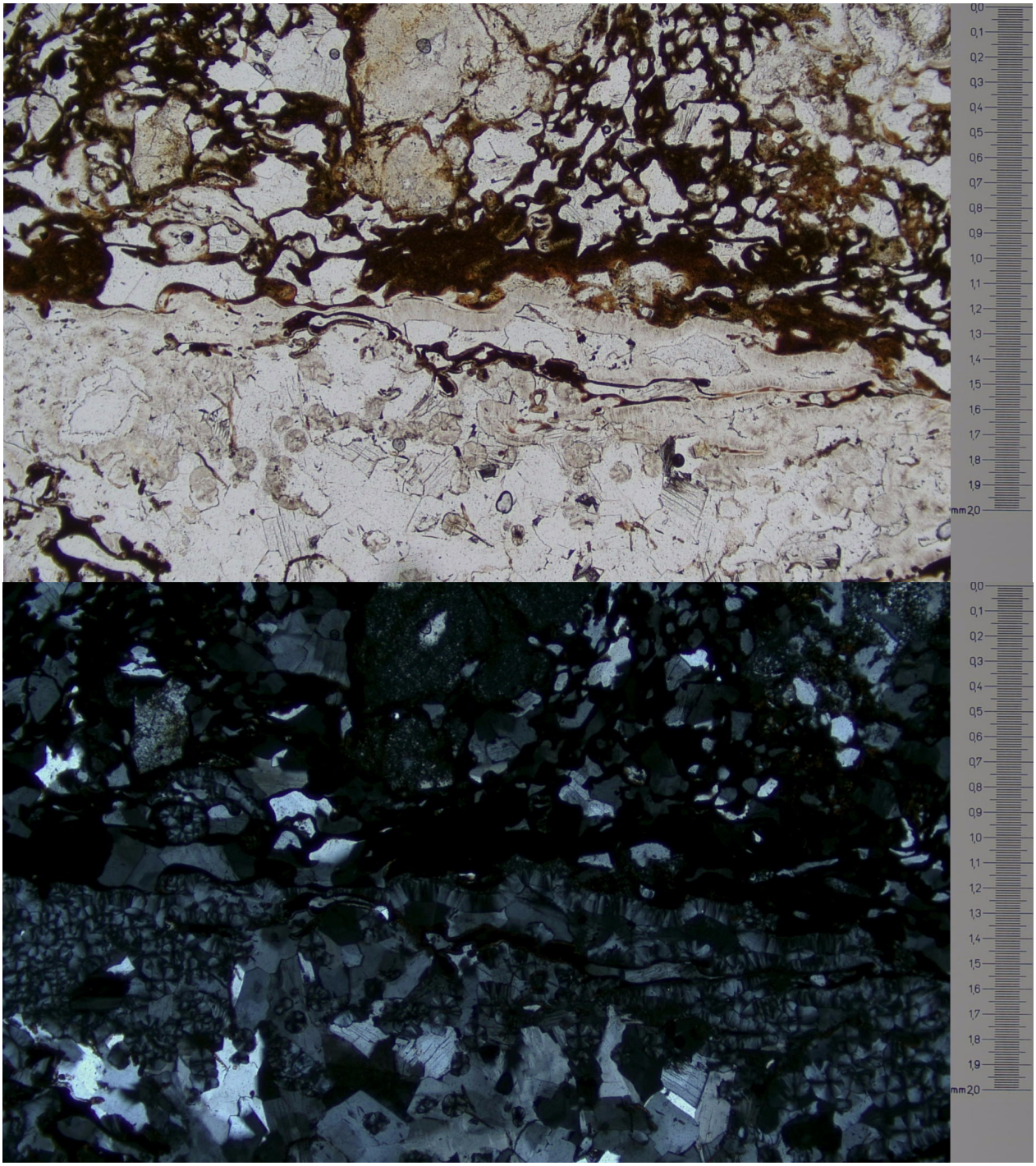

Appendix figure 15. Photos taken in PPL on top and XPL on bottom at 4x magnification. The photo shows the melt-crystal interface of the central clast (found in the lower half of the image) to outside melt (upper half) in 3YB. In the central clast, many spherulites and axiolites can be seen, while none are found outside of the actual clast.

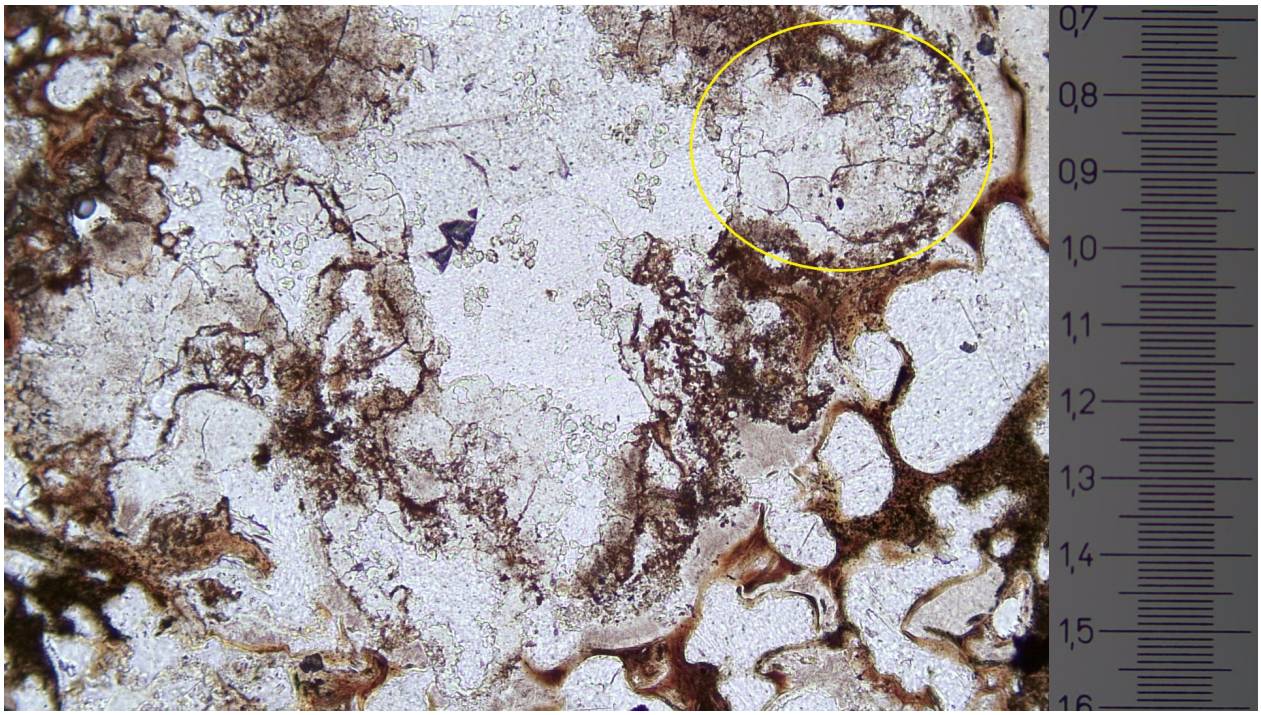

Appendix figure 16. Photo taken in PPL at 10x magnification. In the top right quadrant, ballen quartz textures are circled in yellow. Brown colour signifies glass, while pale green is a sign of amorphized feldspar or quartz, often together and often in the shape of spherulites. The photo was taken in the melt-crystal interface of the central clast in thin section 3YB.

Thin section 3AG

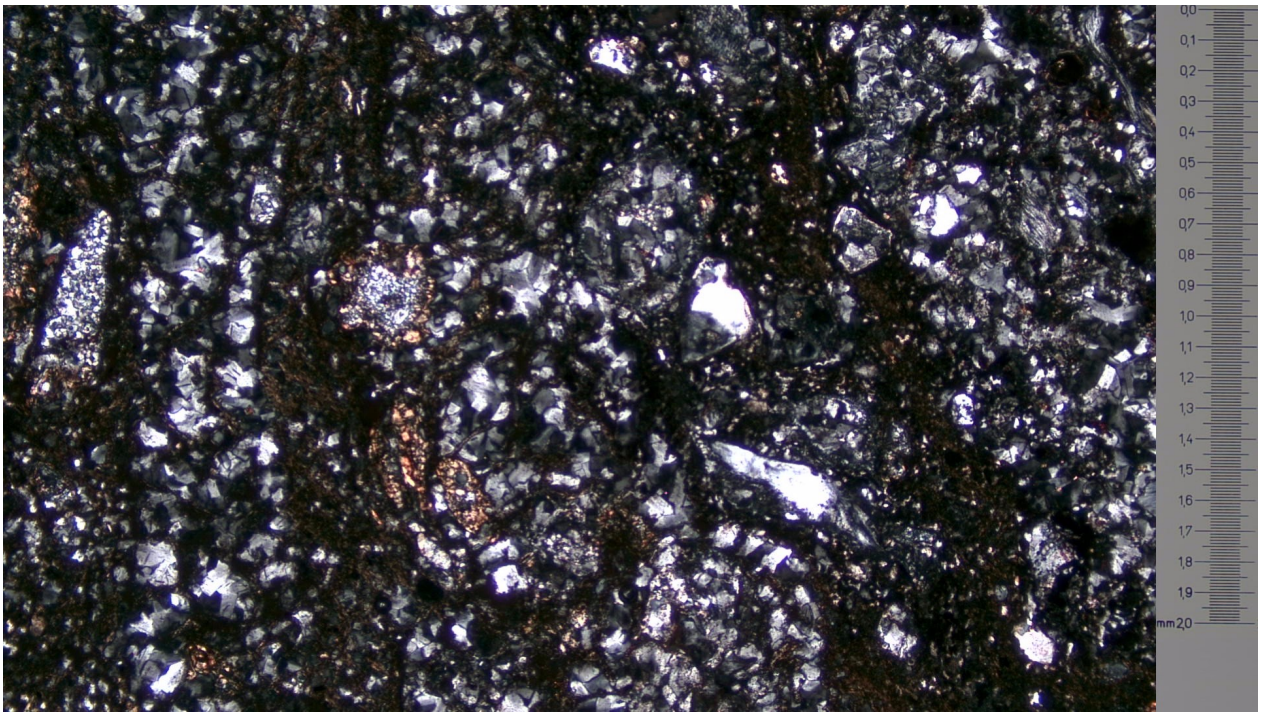

Appendix figure 17. Photo from thin section 3AG in XPL taken at 4x magnification. Most quartz has recrystallized or melted, and melt channels have formed, appearing as dark regions of reduced crystal sizes, passing top to bottom.

Others

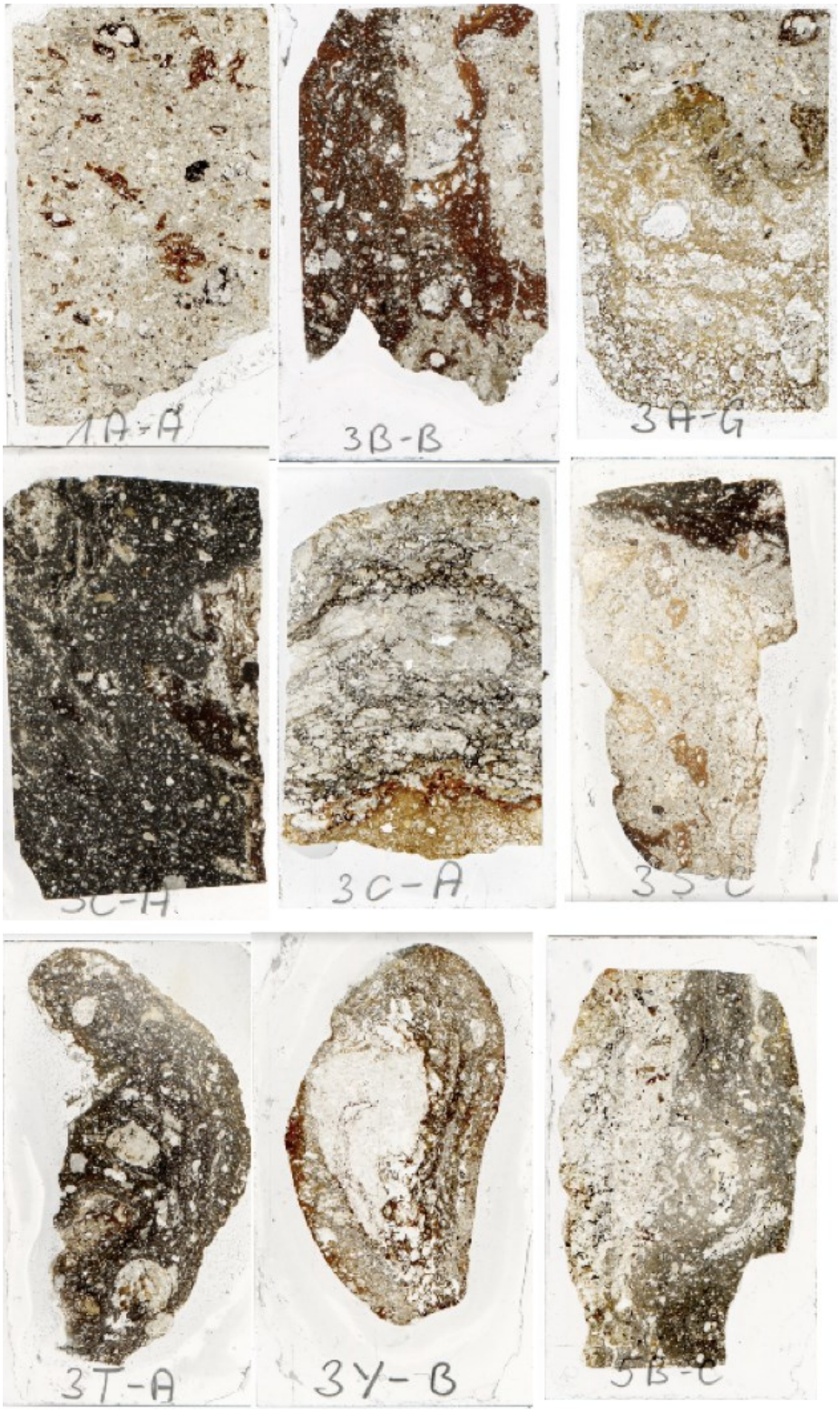

Appendix figure 18. photos of all nine thin sections used in the study in the order; 1AA, 3BB, 3AG, 3CH, 3CA, 3SC, 3TA, 3YB, 5BC.

Tidigare skrifter i serien ”Examensarbeten i Geologi vid Lunds universitet”:

593. Agudelo Motta, Laura Catalina, 2020: Methods for rockfall risk assessment and estimation of runout zones: A case study in Gothenburg, SW Sweden. (45 hp)
594. Johansson, Jonna, 2020: Potentiella nedslagskratrar i Sverige med fokus på Östersjön och östkusten. (15 hp)
595. Haag, Vendela, 2020: Studying magmatic systems through chemical analyses on clinopyroxene - a look into the history of the Teno ankaramites, Tenerife. (45 hp)
596. Kryffin, Isidora, 2020: Kan benceller bevaras över miljontals år? (15 hp)
597. Halvarsson, Ellinor, 2020: Sökande efter nedslagskratrar i Sverige, med fokus på avtryck i berggrunden. (15 hp)
598. Jirdén, Elin, 2020: Kustprocesser i Arktis – med en fallstudie på Prins Karls Forland, Svalbard. (15 hp)
599. Chonewicz, Julia, 2020: The Eemian Baltic Sea hydrography and paleoenvironment based on foraminiferal geochemistry. (45 hp)
600. Paradeisis-Stathis, Savvas, 2020: Holocene lake-level changes in the Siljan Lake District – Towards validation of von Post’s drainage scenario. (45 hp)
601. Johansson, Adam, 2020: Groundwater flow modelling to address hydrogeological response of a contaminated site to remediation measures at Hjortsberga, southern Sweden. (15 hp)
602. Barrett, Aodhan, 2020: Major and trace element geochemical analysis of norites in the Hakefjorden Complex to constrain magma source and magma plumbing systems. (45 hp)
603. Lundqvist, Jennie, 2020: ”Man fyller det med information helt enkelt”: en fenomenografisk studie om studenters upplevelse av geologisk tid. (45 hp)
604. Zachén, Gabriel, 2020: Classification of four mesosiderites and implications for their formation. (45 hp)
605. Viðarsdóttir, Halla Margrét, 2020: Assessing the biodiversity crisis whitin the Triassic-Jurassic boundary interval using redox sensitive trace metals and stable carbon isotope geochemistry. (45 hp)
606. Tan, Brian, 2020: Nordvästra Skånes prekambriska geologiska utveckling. (15 hp)
607. Taxopoulou, Maria Eleni, 2020: Metamorphic micro-textures and mineral assemblages in orthogneisses in NW Skåne – how do they correlate with technical properties? (45 hp)
608. Damber, Maja, 2020: A palaeoecological study of the establishment of beech forest in Söderåsen National Park, southern Sweden. (45 hp)
609. Karastergios, Stylianos, 2020: Characterization of mineral parageneses and metamorphic textures in eclogite- to high-pressure granulite-facies marble at Allmenningen, Roan, western Norway. (45 hp)
610. Lindberg Skutsjö, Love, 2021: Geologiska och hydrogeologiska tolkningar av SkyTEM-data från Vombsänkan, Sjöbo kommun, Skåne. (15 hp)
611. Hertzman, Hanna, 2021: Odensjön - A new varved lake sediment record from southern Sweden. (45 hp)
612. Molin, Emmy, 2021: Rare terrestrial vertebrate remains from the Pliensbachian (Lower Jurassic) Hasle Formation on the Island of Bornholm, Denmark. (45 hp)
613. Höjbert, Karl, 2021: Dendrokronologi - en nyckelmetod för att förstå klimat- och miljöförändringar i Jämtland under holocen. (15 hp)
614. Lundgren Sassner, Lykke, 2021: A Method for Evaluating and Mapping Terrestrial Deposition and Preservation Potential- for Palaeostorm Surge Traces. Remote Mapping of the Coast of Scania, Blekinge and Halland, in Southern Sweden, with a Field Study at Dalköpinge Ängar, Trelleborg. (45 hp)
615. Granbom, Johanna, 2021: En detaljerad undersökning av den mellanordoviciska ”furudalkalkstenen” i Dalarna. (15 hp)
616. Greiff, Johannes, 2021: Oolites from the Arabian platform: Archives for the aftermath of the end-Triassic mass extinction. (45 hp)
617. Ekström, Christian, 2021: Rödfärgade utfällningar i dammanläggningar orsakade av *G. ferruginea* och *L. ochracea* - Problemstatistik och mikrobiella levnadsförutsättningar. (15 hp)
618. Östsjö, Martina, 2021: Geologins betydelse i samhället och ett första steg mot en geopark på Gotland. (15 hp)
619. Westberg, Märta, 2021: The preservation of cells in biomineralized vertebrate tissues of Mesozoic age – examples from a Cretaceous mosasaur (Reptilia, Mosasauridae). (45 hp)
620. Gleisner, Lovisa, 2021: En detaljerad undersökning av kalkstenslager i den mellanordoviciska gullhögenformationen på Billingen i Västergötland. (15 hp)
621. Bonnevier Wallstedt, Ida, 2021: Origin and early evolution of isopods - exploring morphology, ecology and systematics. (15 hp)

622. Selezeneva, Natalia, 2021: Indications for solar storms during the Last Glacial Maximum in the NGRIP ice core. (45 hp)
623. Bakker, Aron, 2021: Geological characterisation of geophysical lineaments as part of the expanded site descriptive model around the planned repository site for high-level nuclear waste, Forsmark, Sweden. (45 hp)
624. Sundberg, Oskar, 2021: Jordlagerföljden i Höjeådalen utifrån nya borrningar. (15 hp)
625. Sartell, Anna, 2021: The igneous complex of Ekmanfjorden, Svalbard: an integrated field, petrological and geochemical study. (45 hp)
626. Juliusson, Oscar, 2021: Implications of ice-bedrock dynamics at Ullstorp, Scania, southern Sweden. (45 hp)
627. Eng, Simon, 2021: Rödslam i svenska kraftdammar - Problematik och potentiella lösningar. (15 hp)
628. Kervall, Hanna, 2021: Feasibility of Enhanced Geothermal Systems in the Precambrian crystalline basement in SW Scania, Sweden. (45 hp)
629. Smith, Thomas, 2022: Assessing the relationship between hypoxia and life on Earth, and implications for the search for habitable exoplanets. (45 hp)
630. Neumann, Daniel, 2022: En mosasaurie (Reptilia, Mosasauridae) av paleocensk ålder? (15 hp)
631. Svensson, David, 2022: Geofysisk och geologisk tolkning av kritskollors utbredning i Ystadsområdet. (15 hp)
632. Allison, Edward, 2022: Avsättning av Black Carbon i sediment från Odensjön, södra Sverige. (15 hp)
633. Jirdén, Elin, 2022: OSL dating of the Mesolithic site Nilsvikdalen 7, Bjorøy, Norway. (45 hp)
634. Wong, Danny, 2022: GIS-analys av effekten vid stormflod/havsnivåhöjning, Morupstrakten, Halland. (15 hp)
635. Lycke, Björn, 2022: Mikroplast i vattenavsatta sediment. (15 hp)
636. Schönherr, Lara, 2022: Grön fältspat i Varbergskomplexet. (15 hp)
637. Funck, Pontus, 2022: Granens ankomst och etablering i Skandinavien under postglacial tid. (15 hp)
638. Brotzen, Olga M., 2022: Geologiska besöksmål och geoparker som plattform för popularisering av geovetenskap. (15 hp)
639. Lodi, Giulia, 2022: A study of carbon, nitrogen, and biogenic silica concentrations in *Cyperus papyrus*, the sedge dominating the permanent swamp of the Okavango Delta, Botswana, Africa. (45 hp)
640. Nilsson, Sebastian, 2022: PFAS- En sammanfattning av ny forskning, med ett fokus på föroreningskällor, provtagning, analysmetoder och saneringsmetoder. (15 hp)
641. Jägfeldt, Hans, 2022: Molnens påverkan på jordens strålningsbalans och klimatsystem. (15 hp)
642. Sundberg, Melissa, 2022: Paleontologiska egenskaper och syreisotopsutveckling i borrkärnan Limhamn-2018: Kopplingar till klimatförändringar under yngre krita. (15 hp)
643. Bjermo, Tim, 2022: A re-investigation of hummocky moraine formed from ice sheet decay using geomorphological and sedimentological evidence in the Vomb area, southern Sweden. (45 hp)
644. Halvarsson, Ellinor, 2022: Structural investigation of ductile deformations across the Frontal Wedge south of Lake Vättern, southern Sweden. (45 hp)
645. Brakebusch, Linus, 2022: Record of the end-Triassic mass extinction in shallow marine carbonates: the Lorüns section (Austria). (45 hp)
646. Wahlquist, Per, 2023: Stratigraphy and palaeoenvironment of the early Jurassic volcaniclastic strata at Djupadalsmölla, central Skåne, Sweden. (45 hp)
647. Gebremedhin, G. Gebreselassie, 2023: U-Pb geochronology of brittle deformation using LA-ICP-MS imaging on calcite veins. (45 hp)
648. Mroczek, Robert, 2023: Petrography of impactites from the Dellen impact structure, Sweden. (45 hp)

LUNDS UNIVERSITET

Geologiska institutionen
Lunds universitet
Sölvegatan 12, 223 62 Lund